J. Fluid Mech. (2009), *vol.* 627, *pp.* 179–213. © 2009 Cambridge University Press
doi:10.1017/S0022112009005850 Printed in the United Kingdom

Interaction of finite-amplitude waves with vertically sheared current fields

OKEY G. NWOGU†

Deparment of Naval Architecture and Marine Engineering, University of Michigan, Ann Arbor, MI 48109, USA

(Received 25 May 2008 and in revised form 5 January 2009)

A computationally efficient numerical method is developed to investigate nonlinear interactions between steep surface gravity waves and depth-varying ocean currents. The free-surface boundary conditions are used to derive a coupled set of equations that are integrated in time for the evolution of the free-surface elevation and tangential component of the fluid velocity at the free surface. The vector form of Green's second identity is used to close the system of equations. The closure relationship is consistent with Helmholtz's decomposition of the velocity field into rotational and irrotational components. The rotational component of the flow field is given by the Biot–Savart integral, while the irrotational component is obtained from an integral of a mixed distribution of sources and vortices over the free surface. Wave-induced changes to the vorticity field are modelled using the vorticity transport equation. For weak currents, an explicit expression is derived for the wave-induced vorticity field in Fourier space that negates the need to numerically solve the vorticity transport equation. The computational efficiency of the numerical scheme is further improved by expanding the kernels of the boundary and volume integrals in the closure relationship as a power series in a wave steepness parameter and using the fast Fourier transform method to evaluate the leading-order contribution to the convolution integrals. This reduces the number of operations at each time step from $O(N^2)$ to $O(N\log N)$ for the boundary integrals and $O[(NM)^2]$ to $O(N\log N)$ for the volume integrals, where N is the number of horizontal grid points and M is the number of vertical layers, making the model an order of magnitude faster than traditional boundary/volume integral methods. The numerical model is used to investigate nonlinear wave–current interaction in depth-uniform current fields and the modulational instability of gravity waves in an exponentially sheared current in deep water. The numerical results demonstrate that the mean flow vorticity can significantly affect the growth rate of extreme waves in narrowband sea states.

1. Introduction

Most ocean currents from wind-generated currents in deep water to tidal currents in shallow coastal waters exhibit some degree of shear in the vertical direction. Numerous theoretical studies of surface gravity wave interaction with vertically sheared currents are documented in comprehensive reviews by Peregrine (1976) and Jonsson (1990). One of the earliest studies was by Benjamin (1962) who investigated solitary wave propagation over currents with an arbitrary vorticity distribution. Additional studies

† Email address for correspondence: onwogu@umich.edu

https://doi.org/10.1017/S0022112009005850 Published online by Cambridge University Press

of long-wave propagation over flows with vorticity include Freeman & Johnson (1970) who derived a modified Korteweg–deVries (KdV) equation and Shen (2001) who derived modified Boussinesq-type evolution equations.

For waves in deep or finite water depth, most studies of wave interaction with rotational flows have focused on linear shear flows with constant vorticity. This is primarily due to the considerable simplification of the problem for the constant-vorticity case. Two-dimensional irrotational wave perturbations to a linear shear current field remain irrotational, and most of the existing irrotational wave theories can easily be extended to the constant-vorticity case. Tsao (1959) used a Stokes-type perturbation expansion method to develop a third-order theory for weakly nonlinear waves on linear shear currents. Variants of Stokes-type perturbation theories for linear shear currents have also been developed by Brevik (1979), Kishida & Sobey (1988) and others. Dalrymple (1974) solved the fully nonlinear boundary value problem for large-amplitude waves on linear shear currents, using the Fourier series approximation method. Fully nonlinear numerical solutions of periodic waves on constant-vorticity flows have also been obtained by Simmen & Saffman (1985) for deep water and Teles da Silva & Peregrine (1988) for finite water depth, using the boundary-integral equation method. Computations were carried out for steep waves up to the limiting wave height. Several interesting wave shapes were predicted including symmetric overhanging waves.

Compared to the constant-vorticity case, the computation of surface wave propagation over arbitrarily sheared current profiles is considerably more difficult, since the wave field is no longer irrotational. In general, the governing equations have to be solved by discretizing the fluid volume as opposed to only the boundaries. Dalrymple (1977) proposed an approach for two-dimensional wave fields that uses the Dubreil-Jacotin transformation to map a fluid region bounded by an unknown free surface onto a rectangular domain. The mapping transforms the Poisson equation for the stream function into a nonlinear partial differential equation for the free surface. A finite-difference scheme was then used to solve the transformed equation on a rectangular grid. The Dubreil-Jacotin transformation technique has also been used by Thomas (1990) and Ko & Krauss (2008). A simpler second-order theory for small-amplitude waves interacting with weak currents of arbitary shear was developed by Swan & James (2001).

In this paper, a fully nonlinear system of equations is derived to describe the three-dimensional interaction of steep gravity waves with ocean currents with an arbitrary distribution of vorticity in water of arbitary depth. The nonlinear kinematic and dynamic free-surface boundary conditions are initially rewritten as a set of evolution of the free-surface elevation and tangential component of the fluid velocity at the free surface. A velocity-based boundary-integral formulation is used to close the system of equations and relate the normal velocity at the free surface to the tangential velocity and wave-induced rotational flow field. The velocity field at any point in the fluid domain is represented by a distribution of point sources and vortices on the free surface, whose strengths are respectively proportional to the normal and tangential velocities at the free surface, and a distribution of point vortices in fluid domain, whose strengths are proportional to the wave-induced vorticity distribution.

The closure relationship is a Fredholm integral equation of the second kind with a diagonally dominant structure that is efficiently solved using an iterative method. The computations are further accelerated for non-overturning waves in which the boundary/volume integrals reduce to convolutions in the horizontal plane. To speed up evaluation of the convolution integrals, we adopt the approach of Clamond &

https://doi.org/10.1017/S0022112009005850 Published online by Cambridge University Press

Grue (2001) and expand the convolution integrals as a power series in a wave steepness parameter with an explicit remainder term. This is equivalent to rewriting the integrals as a summation of far-field terms that decay slowly in space and near-field terms that decay more rapidly in space. The fast Fourier transform (FFT) method is then used to efficiently evaluate the leading-order (far-field) contributions to the convolution integrals.

The numerical model is used to investigate the modulational instability (Benjamin & Feir 1967) of finite-amplitude waves in the presence of vertically sheared currents. Several laboratory experiments have reported conflicting observations on the effect of surface winds and wind-generated currents on the stability of deep-water waves. Bliven, Huang & Long (1986) found a decrease in the sideband amplitudes and growth rates with increasing wind speed, while Li, Hui & Donelan (1988) observed an enhancement of sideband growth rates in light winds but suppression under strong winds. Waseda & Tulin (1999) found a more complex relationship between wind speed and the sideband growth rates. When the sideband amplitudes were initially seeded, the sideband growth rates first decreased before increasing with increasing wind speed. Unseeded experiments, however, showed an increase of the growth rate for all wind speeds in contrast to the findings of Bliven *et al.* (1986) and Li *et al.* (1988).

Li *et al.* (1988) considered the dominant effect of wind to be due to the vertical shear of wind-induced currents and developed a modified nonlinear Schrodinger equation for waves propagating over a linear shear current. Their numerical results showed that a small -velocity shear (corresponding to lighter wind conditions) enhanced instability, while a high-velocity shear (stronger wind) suppressed instability in qualitative agreement with their experimental findings. Baumstein (1998) attempted to model more realistic surface ocean current profiles with a piecewise linear velocity profile. His results also showed that the vertical shear in the mean flow initially enhances instability before suppressing it at higher vorticities.

In this paper, the nonlinear wave–current interaction model is used to investigate the effect of vorticity of the mean flow on the instability of finite-amplitude deep-water waves. A set of coupled equations for the evolution of the free-surface elevation, tangential velocity at the free surface and vorticity field for fully nonlinear waves propagating over an arbitrarily sheared current field is derived in § 2. The velocity-based boundary-integral formulation that is used to close the system of equations is described in § 3. The linear dispersive properties of the equations are investigated in § 4 and found to be consistent with previous results from the Rayleigh equation. The computationally efficient FFT-based numerical solution scheme is described in § 5. In § 6, we present numerical results of finite-amplitude wave interaction with depth-uniform currents and the modulational instability of finite-amplitude waves in vertically sheared current fields. Finally, the concluding remarks are presented in § 7.

2. Derivation of evolution equations

Consider three-dimensional unsteady gravity wave perturbations $\boldsymbol{u}(x, y, z, t) = (u, v, w)$ to a steady vertically sheared current field $\boldsymbol{U}(z) = (U, V, 0)$. A fixed Cartesian coordinate system is adopted with (x, y), the horizontal plane at the still water level and z measured vertically upwards as shown in figure 1. The free-surface elevation is denoted by $\eta(x, y, t)$, while the water depth is denoted by h. The fluid is assumed to be incompressible and inviscid. The wave motions are governed by the continuity

https://doi.org/10.1017/S0022112009005850 Published online by Cambridge University Press

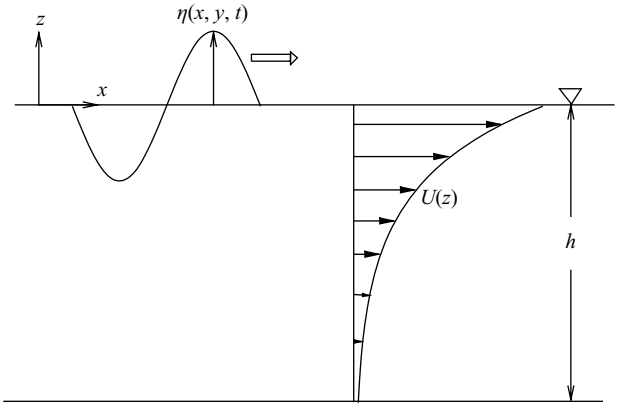


FIGURE 1. Definition sketch.

and Euler equations:

$$\nabla \cdot \boldsymbol{u} = 0, \tag{2.1}$$

$$u_t + (u+U)u_x + (v+V)u_y + wu_z + wU' + \frac{1}{\rho}p_x = 0, \tag{2.2}$$

$$v_t + (u+U)v_x + (v+V)v_y + wv_z + wV' + \frac{1}{\rho}p_y = 0, \tag{2.3}$$

$$w_t + (u+U)w_x + (v+V)w_y + ww_z + g + \frac{1}{\rho}p_z = 0, \tag{2.4}$$

where p is the fluid pressure; g is the gravitational acceleration; ρ is the fluid density; and $\nabla = (\partial/\partial x, \partial/\partial y, \partial/\partial z)$ is the three-dimensional gradient operator. The fluid also has to satisfy the usual kinematic and dynamic boundary conditions at the free surface,

$$\eta_t = w_\eta - (u_\eta + U_\eta)\,\eta_x - (v_\eta + V_\eta)\,\eta_y, \tag{2.5}$$

$$p(x, y, \eta, t) = 0, \tag{2.6}$$

and the kinematic boundary condition at the seabed,

$$w(x, y, -h, t) = 0, \tag{2.7}$$

where $\boldsymbol{u}_\eta = \boldsymbol{u}(x, y, \eta, t)$ and $\boldsymbol{U}_\eta = \boldsymbol{U}(\eta)$ are respectively the wave and current velocities at the free surface. The nonlinear boundary conditions at the free surface can be rewritten as a set of evolution equations for the free-surface elevation and tangential velocity at the free surface. McDonald & Witting (1984) derived an evolution equation for the tangential velocity in two-dimensional (vertical plane) free-surface problems and demonstrated that the resulting equation reduces to Kelvin's circulation theorem when integrated over closed regions. Here, we generalize their approach to three-dimensional wave–current problems. Given a free surface $z = \eta$ with outward normal vector $\boldsymbol{n} = (-\eta_x, -\eta_y, 1)/\sqrt{1+\eta_x^2+\eta_y^2}$, the normal and tangential components of the fluid velocity at the free surface can be written as

$$\boldsymbol{u}\cdot\boldsymbol{n}|_\eta = \frac{1}{\sqrt{1+\eta_x^2+\eta_y^2}}\,(w_\eta - u_\eta\eta_x - v_\eta\eta_y), \tag{2.8}$$

$$\boldsymbol{u}\times\boldsymbol{n}|_\eta = \frac{1}{\sqrt{1+\eta_x^2+\eta_y^2}}\,(v_\eta + w_\eta\eta_y, -u_\eta - w_\eta\eta_x, v_\eta\eta_x - u_\eta\eta_y), \tag{2.9}$$

https://doi.org/10.1017/S0022112009005850 Published online by Cambridge University Press

where the tangential velocity components are defined in the $(yz,\ zx,\ xy)$ planes. We choose the independent velocity variables to be $(u_s,\ v_s)$, which are the horizontal components of the scaled tangential velocity vector at the free surface:

$$u_s = u_\eta + w_\eta \eta_x \tag{2.10}$$

$$v_s = v_\eta + w_\eta \eta_y. \tag{2.11}$$

We also define a normal velocity variable u_n which is the scaled normal velocity at the free surface:

$$u_n = w_\eta - u_\eta \eta_x - v_\eta \eta_y\ . \tag{2.12}$$

The fluid velocity at the free surface can be uniquely defined in terms of either (u_η, v_η, w_η) or (u_s, v_s, u_n). Given u_s, v_s and u_n, (2.10)–(2.12) can be inverted to retrieve (u_η, v_η, w_η):

$$u_\eta = u_s - \frac{\eta_x}{1+\eta_x^2+\eta_y^2}\,(u_n + u_s\eta_x + v_s\eta_y), \tag{2.13}$$

$$v_\eta = v_s - \frac{\eta_y}{1+\eta_x^2+\eta_y^2}\,(u_n + u_s\eta_x + v_s\eta_y), \tag{2.14}$$

$$w_\eta = \frac{1}{1+\eta_x^2+\eta_y^2}\,(u_n + u_s\eta_x + v_s\eta_y). \tag{2.15}$$

The kinematic free-surface boundary condition (2.5) can be written directly in terms of normal velocity variable, u_n, as

$$\eta_t = u_n - U_\eta \eta_x - V_\eta \eta_y\ . \tag{2.16}$$

The evolution equations for the tangential velocities at the free surface are obtained by evaluating the Euler equations at the free surface. In order recast the momentum equations as a set of evolution equations, we make extensive use of the chain rule of differentiation (e.g. McDonald & Witting 1984):

$$\frac{\partial f_\eta}{\partial t} = \left(\frac{\partial f}{\partial t} + \frac{\partial f}{\partial z}\eta_t\right)\bigg|_\eta\ , \tag{2.17}$$

$$\frac{\partial f_\eta}{\partial x_j} = \left(\frac{\partial f}{\partial x_j} + \frac{\partial f}{\partial z}\frac{\partial \eta}{\partial x_j}\right)\bigg|_\eta\ , \tag{2.18}$$

where $f_\eta = f(x, y, \eta, t)$ is used to denote the value a variable of interest $(p, u, v$ or $w)$ at the free surface and $(x_1, x_2) = (x, y)$. Equation (2.18) is initially used to recast the dynamic free-surface boundary condition (2.6) as

$$\frac{\partial p}{\partial x_j}\bigg|_\eta + \frac{\partial p}{\partial z}\bigg|_\eta \frac{\partial \eta}{\partial x_j} = 0\ , \tag{2.19}$$

since $p_\eta = 0$. Substituting the pressure gradients from the Euler equations ((2.2)–(2.4)) into (2.19), we obtain a coupled set of x and y momentum equations in terms of the tangential fluid acceleration at the free surface:

$$\begin{aligned} &u_t|_\eta + (u_\eta + U_\eta)\,u_x|_\eta + (v_\eta + V_\eta)\,u_y|_\eta + w_\eta\,u_z|_\eta + w_\eta\,U'|_\eta \\ &\quad + (w_t|_\eta + (u_\eta + U_\eta)\ w_x|_\eta + (v_\eta + V_\eta)\ w_y|_\eta + w_\eta\,w_z|_\eta + g)\eta_x = 0, \end{aligned} \tag{2.20}$$

https://doi.org/10.1017/S0022112009005850 Published online by Cambridge University Press

$$v_t|_\eta + (u_\eta + U_\eta)\ v_x|_\eta + (v_\eta + V_\eta)\ v_y|_\eta + w_\eta\ v_z|_\eta + w_\eta\ V'|_\eta + (w_t|_\eta + (u_\eta + U_\eta)\ w_x|_\eta + (v_\eta + V_\eta)\ w_y|_\eta + w_\eta\ w_z|_\eta + g)\eta_y = 0. \quad (2.21)$$

We now recast (2.20) and (2.21) as a set of evolution equations for the tangential velocities (u_s, v_s) at the free surface. The chain rule and the kinematic free-surface boundary condition (2.5) are initially applied to (2.20) to obtain

$$u_{\eta,t} + w_{\eta,t}\eta_x + g\eta_x + (u_\eta + U_\eta)(u_{\eta,x} + w_{\eta,x}\eta_x) + (v_\eta + V_\eta)(u_{\eta,y} + w_{\eta,y}\eta_x) + w_\eta\ U'|_\eta = 0. \quad (2.22)$$

Substituting (2.10) and (2.11) into (2.22), we obtain an evolution equation for the tangential velocity at the free surface as

$$u_{s,t} + g\eta_x + (u_\eta + U_\eta)\,u_{s,x} + (v_\eta + V_\eta)\,u_{s,y} - w_\eta w_{\eta,x} + w_\eta(U'|_\eta + u_{\eta,x}\eta_x + v_{\eta,x}\eta_y) = 0. \quad (2.23)$$

The evolution equation can also be written as

$$u_{s,t} + \left[g\ \eta + \frac{1}{2}\left(u_s^2 + v_s^2\right) - \frac{1}{2}w_\eta^2\left(1 + \eta_x^2 + \eta_y^2\right)\right]_x - (v_s - w_\eta\eta_y)(v_{s,x} - u_{s,y}) + w_\eta\ U'|_\eta + U_\eta u_{s,x} + V_\eta u_{s,y} = 0. \quad (2.24)$$

A similar evolution equation can be obtained for the tangential velocity in the y direction

$$v_{s,t} + \left[g\ \eta + \frac{1}{2}\left(u_s^2 + v_s^2\right) - \frac{1}{2}w_\eta^2\left(1 + \eta_x^2 + \eta_y^2\right)\right]_y + (u_s - w_\eta\eta_x)(v_{s,x} - u_{s,y}) + w_\eta\ V'|_\eta + U_\eta v_{s,x} + V_\eta v_{s,y} = 0. \quad (2.25)$$

The evolution equations for the tangential velocities (2.24) and (2.25) do not explicitly depend on the vorticity distribution. However, the vertical profile of the current is required in the closure relationship between the normal and tangential velocities at the free surface, as discussed later in § 3.

For irrotational flows without currents, Zakharov (1968) recast the free-surface boundary conditions as a Hamiltonian system with the free-surface elevation and velocity potential at the free surface (ϕ_η) as canonical variables. This formulation is commonly used in higher order spectral models (e.g. Dommermuth & Yue 1987; West *et al.* 1987; Choi 1995). The dynamic free-surface boundary condition is given in terms ϕ_η as

$$\phi_{\eta,t} + g\eta + \frac{1}{2}\left[\phi_{\eta,x}^2 + \phi_{\eta,y}^2\right] - \frac{1}{2}w_\eta^2\left(1 + \eta_x^2 + \eta_y^2\right) = 0. \quad (2.26)$$

We note that the irrotational form of evolution equation for the tangential velocity at the free surface (2.24) can also be obtained by taking the horizontal gradient of (2.26), since $u_s = \partial\phi_\eta/\partial x$ and $v_s = \partial\phi_\eta/\partial y$ (e.g. Madsen, Bingham & Liu 2002; Fructus *et al.* 2005).

The evolution of the vorticity field due to wave–current interaction is governed by the vorticity transport equations, which are obtained by taking the curl of the Euler equations (2.2)–(2.4):

$$\Omega_{1,t} + (u + U)\,\Omega_{1,x} + (v + V)\,\Omega_{1,y} + w\Omega_{1,z} - \Omega_1 u_x - \Omega_2 u_y - \Omega_3 u_z = U'v_x - V'u_x + wV'', \quad (2.27)$$

https://doi.org/10.1017/S0022112009005850 Published online by Cambridge University Press

$$\Omega_{2,t} + (u+U)\,\Omega_{2,x} + (v+V)\,\Omega_{2,y} + w\Omega_{2,z} - \Omega_1 v_x - \Omega_2 v_y - \Omega_3 v_z = U' v_y - V' u_y - wU'', \quad (2.28)$$

where $\boldsymbol{\Omega}(x, y, z, t) = (\Omega_1, \Omega_2, \Omega_3)$ is the vorticity vector defined as

$$\boldsymbol{\Omega} = \nabla \times \boldsymbol{u} = (w_y - v_z, u_z - w_x, v_x - u_y). \quad (2.29)$$

The terms on the right-hand side of (2.27) and (2.27) explicitly describe how the wave orbital velocity field interacts with the current field to redistribute vorticity. The first two terms describe stretching of vortices by gradients of the horizontal wave velocity field, while the last term describes coupling of the vertical orbital wave velocity (w) with the vorticity gradients in the mean flow (U'', V''). In two-dimensional (vertical plane) flow fields with linear shear currents ($U'' = 0$), the vorticity production terms reduce to zero, and the wave motion remains irrotational (Tsao 1959).

Equations (2.16), (2.24), (2.25), (2.27) and (2.27) represent a complete set of equations that govern the time-dependent evolution of the free-surface elevation, tangential velocities at the free surface and vorticity field. The equations are valid for non-breaking waves of arbitrary steepness and flows with an arbitrary horizontal vorticity distribution. To close the system of equations, we need to determine the relationship between the free-surface elevation, η, normal velocity, u_n, tangential velocities (u_s, v_s) and vorticity distribution. For irrotational waves in shallow water, the system of equations can be closed by expanding the velocity field as a Taylor series about an arbitrary point in the water column (e.g. Nwogu 1993). Other methods of closing the equations for water of arbitrary depth include a Stokes-type asymptotic expansion for weakly nonlinear wave fields (e.g. West *et al.* 1987) and the boundary-integral method for highly nonlinear wave fields (e.g. Longuet-Higgins & Cokelet 1976). In this paper, we adopt the boundary-integral approach for fully nonlinear waves in water of arbitrary depth. In order to allow for flows with arbitrary vorticity, the vector form of Green's second identity is used to derive a boundary/volume integral equation in terms of the fluid velocities instead of the more commonly used velocity potential.

3. Velocity-based boundary-integral closure relationship

3.1. *Free-space Green's function*

The velocity field in a rotational flow with vorticity vector, $\boldsymbol{\Omega}$, is governed by the Poisson equation

$$\nabla^2 \boldsymbol{u} = \nabla(\nabla \cdot \boldsymbol{u}) - \nabla \times (\nabla \times \boldsymbol{u}) = -\nabla \times \boldsymbol{\Omega}. \quad (3.1)$$

The solution of (3.1) in an unbounded fluid can be directly written in terms of a convolution of the curl of the vorticity field with a Green's function,

$$\boldsymbol{u}(\boldsymbol{x}) = -\int\int\int G(\boldsymbol{x}; \boldsymbol{x}')\,(\nabla' \times \boldsymbol{\Omega}(\boldsymbol{x}'))\,\mathrm{d}\boldsymbol{x}', \quad (3.2)$$

where $\boldsymbol{x}$ is the field point at which the velocity is evaluated; $\boldsymbol{x}'$ is the location of point sources; and $\nabla' = (\partial/\partial x', \partial/\partial y', \partial/\partial z')$ denotes the gradient operator with respect to $\boldsymbol{x}'$. The Green's function represents the fundamental solution to the homogenous part of the governing equation (3.1) and is given by

$$G(\boldsymbol{x};\ \boldsymbol{x}') = \begin{cases} -\dfrac{1}{4\pi\,|\boldsymbol{x} - \boldsymbol{x}'|} & \text{in three dimensions,} \\ \dfrac{1}{2\pi} \ln|\boldsymbol{x} - \boldsymbol{x}'| & \text{in two dimensions.} \end{cases} \quad (3.3)$$

https://doi.org/10.1017/S0022112009005850 Published online by Cambridge University Press

3.2. *Vector form of Green's identity for bounded regions*

We now consider a bounded fluid region V with a smooth enclosing boundary ∂V. The vector form of Green's second identity may be applied at any instant of time to determine the fluid velocity inside the bounded region from the boundary values of the velocity and a volume integral of the vorticity distribution. Given two vectors $\boldsymbol{P}$ and $\boldsymbol{Q}$ that are at least twice differentiable in V and on ∂V, the vector form of Green's second identity may be written as (see Morse & Feshbach 1953, § 13.1)

$$\int\int_V\int [\boldsymbol{P}\cdot\nabla^2\boldsymbol{Q}-\boldsymbol{Q}\cdot\nabla^2\boldsymbol{P}]\mathrm{d}V=\oint_{\partial V}\{[\boldsymbol{P}\nabla\cdot\boldsymbol{Q}-\boldsymbol{Q}\nabla\cdot\boldsymbol{P}]\cdot\boldsymbol{n} - [\boldsymbol{P}\cdot(\boldsymbol{n}\times(\nabla\times\boldsymbol{Q}))+(\nabla\times\boldsymbol{P})\cdot(\boldsymbol{n}\times\boldsymbol{Q})]\}\mathrm{d}S, \quad (3.4)$$

where $\boldsymbol{n}$ is an outward normal vector to ∂V. By choosing $\boldsymbol{P}$ to be the fluid velocity $\boldsymbol{u}$ and $\boldsymbol{Q}$ to be the product of the scalar Green's function G and the unit vector $\boldsymbol{e}_j$ in the jth coordinate direction we obtain

$$\begin{aligned}\alpha\boldsymbol{u}(\boldsymbol{x})\cdot\boldsymbol{e}_j=&-\int\int_V\int[G(\boldsymbol{x};\boldsymbol{x}')\boldsymbol{e}_j\cdot\nabla'\times\boldsymbol{\Omega}(\boldsymbol{x}')]\,\mathrm{d}V\\&+\oint_{\partial V}(\boldsymbol{u}(\boldsymbol{x}')\cdot\boldsymbol{n}(\boldsymbol{x}'))\nabla'G(\boldsymbol{x};\boldsymbol{x}')\cdot\boldsymbol{e}_j\,\mathrm{d}S\\&-\oint_{\partial V}[(\boldsymbol{u}(\boldsymbol{x}')\times\boldsymbol{n}(\boldsymbol{x}'))\cdot(\nabla'\times[G\boldsymbol{e}_j])\\&-G(\boldsymbol{x};\boldsymbol{x}')[(\nabla'\times\boldsymbol{u}(\boldsymbol{x}'))\times\boldsymbol{n}(\boldsymbol{x}')]\cdot\boldsymbol{e}_j]\,\mathrm{d}S,\end{aligned} \quad (3.5)$$

where use has been made of the vector identity $\boldsymbol{A}\cdot(\boldsymbol{B}\times\boldsymbol{C})=(\boldsymbol{A}\times\boldsymbol{B})\cdot\boldsymbol{C}$. The parameter $\alpha=(1/2,1)$ for points on ∂V and inside V respectively. Given that $\nabla\times[G\boldsymbol{e}_j]=\nabla G\times\boldsymbol{e}_j$, (3.5) can be further reduced to

$$\begin{aligned}\alpha\,\boldsymbol{u}(\boldsymbol{x})=&\oint_{\partial V}[(\boldsymbol{u}(\boldsymbol{x}')\cdot\boldsymbol{n}(\boldsymbol{x}'))\nabla'G(\boldsymbol{x};\,\boldsymbol{x}')-(\boldsymbol{u}(\boldsymbol{x}')\times\boldsymbol{n}(\boldsymbol{x}'))\times\nabla'G(\boldsymbol{x};\,\boldsymbol{x}')]\,\mathrm{d}S\\&-\int\int_V\int G(\boldsymbol{x};\,\boldsymbol{x}')[\nabla'\times\boldsymbol{\Omega}(\boldsymbol{x}')]\mathrm{d}V-\oint_{\partial V}G(\boldsymbol{x};\,\boldsymbol{x}')[\boldsymbol{\Omega}(\boldsymbol{x}')\times\boldsymbol{n}(\boldsymbol{x}')]\,\mathrm{d}S.\end{aligned} \quad (3.6)$$

The velocity field at any point in the fluid region V or on the boundary ∂V can thus be represented by a distribution of point sources on ∂V whose strengths are proportional to the normal velocity $(\boldsymbol{u}\cdot\boldsymbol{n})$ on ∂V, a distribution of point vortices on ∂V whose strengths are proportional to the tangential velocity $(\boldsymbol{u}\times\boldsymbol{n})$ and a distribution of point sources in V and on ∂V whose strengths are proportional to the curl of the vorticity distribution. The normal velocity along the boundary ∂V that is required to close the system of evolution equations is obtained from (3.6) as

$$\begin{aligned}\frac{1}{2}\boldsymbol{u}(\boldsymbol{x})\cdot\boldsymbol{n}(\boldsymbol{x})=&\oint_{\partial V}(\boldsymbol{u}(\boldsymbol{x}')\cdot\boldsymbol{n}(\boldsymbol{x}'))\nabla'G(\boldsymbol{x};\boldsymbol{x}')\cdot\boldsymbol{n}(\boldsymbol{x})\,\mathrm{d}S\\&-\oint_{\partial V}(\boldsymbol{u}(\boldsymbol{x}')\times\boldsymbol{n}(\boldsymbol{x}'))\cdot(\nabla'G(\boldsymbol{x};\boldsymbol{x}')\times\boldsymbol{n}(\boldsymbol{x}))\,\mathrm{d}S+\boldsymbol{U}_{\Omega}(\boldsymbol{x})\cdot\boldsymbol{n}(\boldsymbol{x}),\end{aligned} \quad (3.7)$$

https://doi.org/10.1017/S0022112009005850 Published online by Cambridge University Press

where $\boldsymbol{n}(\boldsymbol{x})$ is the unit normal vector to ∂V at the field point $\boldsymbol{x}$ and $\boldsymbol{U}_\Omega = (U_\Omega, V_\Omega, W_\Omega)$ represents the rotational flow field induced by vorticity-related singularities:

$$\boldsymbol{U}_\Omega(\boldsymbol{x}) = -\int\int_V\int G(\boldsymbol{x};\ \boldsymbol{x}')\,[\nabla' \times \boldsymbol{\Omega}(\boldsymbol{x}')]\,\mathrm{d}V - \oint_{\partial V} G(\boldsymbol{x};\ \boldsymbol{x}')\,[\boldsymbol{\Omega}(\boldsymbol{x}') \times \boldsymbol{n}(\boldsymbol{x}')]\,\mathrm{d}S\ . \quad (3.8)$$

The velocity field induced by the vorticity-related singularities (3.8) may also be recast into the more familiar Biot–Savart form using the divergence theorem (see Appendix A):

$$\boldsymbol{U}_\Omega(\boldsymbol{x}) = -\int\int_V\int \boldsymbol{\Omega}(\boldsymbol{x}') \times \nabla' G(\boldsymbol{x};\ \boldsymbol{x}')\,\mathrm{d}V. \quad (3.9)$$

Although (3.8) and (3.9) are equivalent, (3.8) more clearly illustrates the relative contribution of the mean flow vorticity and vorticity gradients to the velocity field. For flows with constant vorticity, the volume integral in (3.8) reduces to zero, and the flow field is completely described by an integral of the vorticity along the boundaries.

Variants of the velocity-based boundary-integral formulation have been used in numerical studies of viscous flows with the Navier–Stokes equations (e.g. Wu 1984; Morino, Salvatore & Gennaretti 1999), irrotational free-surface flows using the vortex sheet method (e.g. Zaroodny & Greenberg 1973; Baker, Meiron & Orszag 1982; Chen & Vorus 1992) and Cauchy's integral formulation for the complex velocity field (e.g. Vinje & Brevig 1981; Dold 1992). In the classical vortex sheet method, vortex sheets of unknown strength are distributed on the free surface. The vorticity transport equation is then solved for the evolution of the vortex strength. Green's identity approach, however, leads to a mixed distribution of point sources and vortices on the free surface and reduces to Cauchy's integral theorem for two-dimensional flow fields. The source strengths are set *a priori* to the jump in the normal velocity across the free surface, while the vortex sheet strength is set *a priori* to the jump in the tangential velocity across the free surface. The horizontal momentum equations are then solved for the evolution of the tangential velocities.

The closure relationship (3.7) also provides a relatively simple conceptual model for describing the interaction of waves with arbitrarily sheared current fields. The perturbation to the mean velocity field by surface waves can be decomposed into an irrotational component, $\boldsymbol{u}_\phi$, associated with oscillatory wave motions, and a rotational component, $\boldsymbol{U}_\Omega$, related to the unsteady vorticity produced by wave–current interaction:

$$\boldsymbol{u}(\boldsymbol{x}, t) = \boldsymbol{u}_\phi(\boldsymbol{x}, t) + \boldsymbol{U}_\Omega(\boldsymbol{x}, t). \quad (3.10)$$

Wave-induced changes to the rotational flow field are modelled by a surface/volume distribution of singularities whose strengths are proportional to the vorticity obtained by solving the vorticity transport equations (2.27) and (2.28). The normal velocity induced by the vorticity-related singularities is then introduced into the evolution equation for the free-surface elevation.

3.3. *Three-dimensional closure relationship*

We now seek to explicitly express the closure relationship (3.7) in terms of the tangential velocity variables (u_s, v_s) and the normal velocity variable, u_n. The boundary of the computational domain, ∂V, consists of the free surface, lateral radiation boundaries and the seabed. Since the water depth is assumed to be constant, the seabed is excluded from ∂V by placing image sources along a reflected sea surface

https://doi.org/10.1017/S0022112009005850 Published online by Cambridge University Press

$\tilde{\eta}(x, y, t)$ at $z = -2h - \eta(x, y, t)$. The image Green's function is given by

$$\tilde{G}(\boldsymbol{x}; \boldsymbol{x}') = \begin{cases} -\dfrac{1}{4\pi\sqrt{(x-x')^2 + (y-y')^2 + (z+z'+2h)^2}} & \text{in three dimensions,} \\ \dfrac{1}{2\pi} \ln \sqrt{(x-x')^2 + (z+z'+2h)^2} & \text{in two dimensions.} \end{cases} \tag{3.11}$$

We assume non-overturning waves and define the two-dimensional horizontal gradient operator $\nabla_h = (\partial/\partial x, \partial/\partial y)$. Substituting $dS = d\boldsymbol{x}'\sqrt{1 + \nabla_h'\eta \cdot \nabla_h'\eta}$ and expressions for the unit normal vectors at $z = \eta$ and $z = -(2h + \eta)$, we obtain

$$\begin{aligned} \frac{1}{2} u_n(\boldsymbol{x}) = & \int_{-\infty}^{\infty} u_n(\boldsymbol{x}') \left(-\nabla_h' G(\boldsymbol{x}, \eta; \boldsymbol{x}', \eta) \cdot \nabla_h \eta(\boldsymbol{x}) + \frac{\partial G}{\partial z'}(\boldsymbol{x}, \eta; \boldsymbol{x}', \eta) \right) \mathrm{d}\boldsymbol{x}' \\ & - \int_{-\infty}^{\infty} u_n(\boldsymbol{x}') \left(\nabla_h' \tilde{G}(\boldsymbol{x}, \eta; \boldsymbol{x}', \tilde{\eta}) \cdot \nabla_h \eta(\boldsymbol{x}) + \frac{\partial \tilde{G}}{\partial z'}(\boldsymbol{x}, \eta; \boldsymbol{x}', \tilde{\eta}) \right) \mathrm{d}\boldsymbol{x}' \\ & - \int_{-\infty}^{\infty} \boldsymbol{u}_s(\boldsymbol{x}') \cdot \left(\nabla_h' G(\boldsymbol{x}, \eta; \boldsymbol{x}', \eta) + \frac{\partial G}{\partial z'}(\boldsymbol{x}, \eta; \boldsymbol{x}', \eta) \nabla_h \eta(\boldsymbol{x}) \right) \mathrm{d}\boldsymbol{x}' \\ & + \int_{-\infty}^{\infty} \boldsymbol{u}_s(\boldsymbol{x}') \cdot \left(\nabla_h' \tilde{G}(\boldsymbol{x}, \eta; \boldsymbol{x}', \tilde{\eta}) - \frac{\partial \tilde{G}}{\partial z'}(\boldsymbol{x}, \eta; \boldsymbol{x}', \tilde{\eta}) \nabla_h \eta(\boldsymbol{x}) \right) \mathrm{d}\boldsymbol{x}' \\ & - \int_{-\infty}^{\infty} (\boldsymbol{u}_s(\boldsymbol{x}') \times \nabla_h \eta(\boldsymbol{x}')) \cdot (\nabla_h' G(\boldsymbol{x}, \eta; \boldsymbol{x}', \eta) \times \nabla_h \eta(\boldsymbol{x})) \, \mathrm{d}\boldsymbol{x}' \\ & - \int_{-\infty}^{\infty} (\boldsymbol{u}_s(\boldsymbol{x}') \times \nabla_h \eta(\boldsymbol{x}')) \cdot (\nabla_h' \tilde{G}(\boldsymbol{x}, \eta; \boldsymbol{x}', \tilde{\eta}) \times \nabla_h \eta(\boldsymbol{x})) \, \mathrm{d}\boldsymbol{x}' \\ & - \boldsymbol{U}_\Omega(\boldsymbol{x}, \eta) \cdot \nabla_h \eta(\boldsymbol{x}) + W_\Omega(\boldsymbol{x}, \eta), \end{aligned} \tag{3.12}$$

where periodicity has been used to eliminate the integrals along the lateral boundaries.

3.4. *Two-dimensional closure relationship*

For two-dimensional (vertical plane) problems, the three-dimensional closure relationship (3.12) reduces to

$$\begin{aligned} u_n(x) = & \frac{1}{\pi} \int_{-\infty}^{\infty} \left\{ \frac{[(x-x')\eta_x - (\eta - \eta')]}{[(x-x')^2 + (\eta - \eta')^2]} + \frac{[(x-x')\eta_x - (\eta + \eta' + 2h)]}{[(x-x')^2 + (\eta + \eta' + 2h)^2]} \right\} u_n(x') \, \mathrm{d}x' \\ & + \frac{1}{\pi} \int_{-\infty}^{\infty} \left\{ \frac{[(x-x') + (\eta - \eta')\eta_x]}{[(x-x')^2 + (\eta - \eta')^2]} - \frac{[(x-x') + (\eta + \eta' + 2h)\eta_x]}{[(x-x')^2 + (\eta + \eta' + 2h)^2]} \right\} u_s(x') \, \mathrm{d}x' \\ & - 2U_\Omega|_{z=\eta} \, \eta_x + 2W_\Omega|_{z=\eta}, \end{aligned} \tag{3.13}$$

where $\eta = \eta(x)$, $\eta' = \eta(x')$ and $\eta_x = \eta_x(x)$. The singular integrals in (3.13) are defined in the Cauchy principal-value sense for integrals involving $1/|x - x'|$ and Hadamard finite-part sense for integrals involving $1/|x - x'|^2$. For small amplitude ($\eta_x \ll 1$) irrotational waves, the two-dimensional closure relationship further simplifies to

$$\begin{aligned} w_0(x) = & -\frac{1}{\pi} \int_{-\infty}^{\infty} \frac{2h}{[(x-x')^2 + 4h^2]} w_0(x') \, \mathrm{d}x' + \frac{1}{\pi} \int_{-\infty}^{\infty} \frac{1}{x - x'} u_0(x') \, \mathrm{d}x' \\ & - \frac{1}{\pi} \int_{-\infty}^{\infty} \frac{(x-x')}{[(x-x')^2 + 4h^2]} u_0(x') \, \mathrm{d}x', \end{aligned} \tag{3.14}$$

https://doi.org/10.1017/S0022112009005850 Published online by Cambridge University Press

where (u_0, w_0) are the horizontal and vertical wave velocities at $z = 0$. In deep water ($h \to \infty$), the linear wave theory relationship between the horizontal and vertical velocities is recovered:

$$w_0(x) = \mathscr{H}[u_0(x)] = \frac{1}{\pi} \int_{-\infty}^{\infty} \frac{1}{x - x'} u_0(x') \, \mathrm{d}x', \tag{3.15}$$

where $\mathscr{H}[\cdot]$ denotes the Hilbert transform. In water of finite depth, we apply the Fourier transform defined as

$$\hat{f}(k) = \mathscr{F}[f(x)] = \int_{-\infty}^{\infty} f(x) \mathrm{e}^{-ikx} \, \mathrm{d}x \tag{3.16}$$

and convolution theorem

$$\mathscr{F}\left[\int_{-\infty}^{\infty} f(x - x') g(x') \, \mathrm{d}x'\right] = \hat{f}(k) \hat{g}(k) \tag{3.17}$$

to (3.14) to obtain

$$\hat{w}_0(k) = -\mathrm{i} \frac{\left(1 - \mathrm{e}^{-2kh}\right)}{\left(1 + \mathrm{e}^{-2kh}\right)} \hat{u}_0(k) = -\mathrm{i} \tanh kh \; \hat{u}_0(k), \tag{3.18}$$

where k is the wavenumber. The exact linear wave theory relationship between the vertical and horizontal velocity at $z = 0$ is thus recovered for water of finite depth.

4. Linear dispersive properties

The Rayleigh equation of hydrodynamic stability theory is often used to describe the dispersive properties of small-amplitude waves propagating over arbitrarily sheared current profiles. The Rayleigh equation can be derived from the vorticity transport equation (2.28) by assuming that the perturbation velocity field (u, w) due to the incident waves is much smaller than the underlying mean flow field $(U, 0)$. For steady waves with phase speed C, (2.28) reduces to

$$(U - C)\Omega_{2,x} = -wU''. \tag{4.1}$$

The preceding equation can also be written in terms of the vertical velocity w. Substituting the definition of Ω_2 in (2.29) to (4.1) and using the continuity equation (2.1) to replace u_{xz} with $-w_{zz}$, we obtain the more familiar form of the Rayleigh equation for the vertical velocity:

$$w_{zz} - k^2 w = \frac{w}{U - C} U'', \tag{4.2}$$

where k is the wavenumber. Explicit analytical solutions of the Rayleigh equation, subject to linearized boundary conditions for w at the free surface and seabed have been obtained by Thompson (1949) and Biesel (1950) for linear shear currents. For arbitrarily sheared profiles in deep water, Shrira (1993) derived a series solution in terms of a non-dimensional vorticity production parameter U''/Ck^2. We now investigate the dispersive properties of the two-dimensional system of evolution and boundary/volume integral equations in the linear limit and compare them to previous analytical solutions.

4.1. *Linear shear current*

Consider a linear shear current with surface velocity U_0 and vorticity U_0':

$$U(z) = U_0 + U_0' z. \tag{4.3}$$

https://doi.org/10.1017/S0022112009005850 Published online by Cambridge University Press

The linearized form of the continuity (2.16) and momentum (2.24) equations for surface wave perturbations to the current field can be written as

$$\eta_t + U_0\eta_x - w_0 = 0, \tag{4.4}$$

$$u_{0,t} + g\ \eta_x + U_0 u_{0,x} + w_0 U_0' = 0, \tag{4.5}$$

where $(u_0,\ w_0)$ are the horizontal and vertical perturbation wave velocities at $z=0$. Since the wave-induced vorticity production term in (4.1) is zero, the closure relationship between u_0 and w_0 is given by (3.14). We initially transform (4.4) and (4.5) to a frame of reference travelling at the wave phase speed, C, and then apply the Fourier transform defined in (3.16) to obtain

$$\mathrm{i}k\,(U_0 - C)\,\hat{\eta}(k) - \hat{w}_0(k) = 0, \tag{4.6}$$

$$\mathrm{i}k\,(U_0 - C)\,\hat{u}_0(k) + \mathrm{i}gk\ \hat{\eta}(k) + U_0'\hat{w}_0(k) = 0, \tag{4.7}$$

$$\hat{w}_0(k) = -\mathrm{i}\tanh kh\ \hat{u}_0(k). \tag{4.8}$$

Equations (4.6)–(4.8) can be combined to yield a dispersion relation for waves propagating on a linear shear current as

$$(U_0 - C)^2 - \frac{U_0'}{k}\tanh kh(U_0 - C) - \frac{g}{k}\tanh kh = 0. \tag{4.9}$$

The foregoing equation is identical to that obtained by Thompson (1949) and corresponds to the exact solution of the Rayleigh equation for linear shear currents. Its solution can be written in the form given by Biesel (1950):

$$C = U_0 - \frac{U_0'}{2k}\tanh kh \pm \sqrt{\left(\frac{U_0'}{2k}\tanh kh\right)^2 + \frac{g}{k}\tanh kh}. \tag{4.10}$$

4.2. *Arbitrarily sheared current profiles*

For current fields with an arbitrary vorticity distribution, the evolution equations remain the same as their constant-vorticity counterparts, with their Fourier transforms given by (4.6) and (4.7). However, U_0' now refers to the vorticity at the still-water level. The perturbation wave velocities also now consist of both rotational and irrotational components. The Fourier transform of the closure relationship (3.13) is given by

$$(1 + \mathrm{e}^{-2kh})\hat{w}_0(k) = -\mathrm{i}(1 - \mathrm{e}^{-2kh})\hat{u}_0(k) + 2\mathscr{F}[W_\Omega|_{z=0}], \tag{4.11}$$

where $W_\Omega|_{z=0}$ is the vertical velocity induced at the still-water level by vorticity-related singularities. Substituting the vorticity transport equation (4.1) into (3.8), we obtain an expression for $W_\Omega|_{z=0}$ as

$$W_\Omega|_{z=0} = \frac{1}{4\pi}\int_{-h}^{0}\int_{-\infty}^{\infty} \ln\left[(x-x')^2 + z'^2\right]\frac{w^{(f)}U''}{(U-C)}\,\mathrm{d}x'\,\mathrm{d}z',$$

$$-\frac{1}{4\pi}\int_{-h}^{0}\int_{-\infty}^{\infty} \ln\left[(x-x')^2 + (z'+2h)^2\right]\frac{w^{(i)}U''}{(U-C)}\,\mathrm{d}x'\,\mathrm{d}z', \tag{4.12}$$

where $w^{(f)}$and $w^{(i)}$ are the vertical velocities associated with the free-space and image Green's function respectively. Since $U''/(U-C)$ is independent of x, we can apply the Fourier convolution theorem to (4.12) to obtain

$$\mathscr{F}[W_\Omega|_{z=0}] = -\frac{1}{2k}\int_{-h}^{0}\left(\mathrm{e}^{kz}\hat{w}^{(f)} - \mathrm{e}^{-k(z+2h)}\hat{w}^{(i)}\right)\frac{U''(z)}{U(z)-C}\,\mathrm{d}z. \tag{4.13}$$

https://doi.org/10.1017/S0022112009005850 Published online by Cambridge University Press

The Fourier transform of the vertical wave velocity in the interior of the flow field is obtained from (3.6) as

$$\hat{w}^{(f)}(k,z) = \hat{w}_0(k)\frac{\mathrm{e}^{kz}}{1-\mathrm{e}^{-2kh}}, \quad \hat{w}^{(i)}(k,z) = -\hat{w}_0(k)\frac{\mathrm{e}^{-k(z+2h)}}{1-\mathrm{e}^{-2kh}}, \tag{4.14}$$

where use has been made of (3.18). Substituting (4.14) and (4.13) into (4.11), we obtain the closure relationship for an arbitrary current profile as

$$\left(1+\frac{1}{k}\int_{-h}^{0}\frac{U''(z)}{U(z)-C}\frac{\cosh 2k(z+h)}{\sinh 2kh}\mathrm{d}z\right)\hat{w}_0(k) = -\mathrm{i}\tanh kh\ \hat{u}_0(k). \tag{4.15}$$

Equations (4.6), (4.7) and (4.15) can be combined to yield the following dispersion relation for waves propagating on arbitrarily sheared currents:

$$\left(1+\frac{1}{k}\int_{-h}^{0}\frac{U''(z)}{U(z)-C}\frac{\cosh 2k(z+h)}{\sinh 2kh}\mathrm{d}z\right)(U_0-C)^2 - \frac{U_0'}{k}\tanh kh\,(U_0-C) - \frac{g}{k}\tanh kh = 0. \tag{4.16}$$

The preceding equation cannot be directly solved for the unknown phase speed, C, since the phase speed also occurs in the denominator of the integral. However, a simplified dispersion relation can be derived if the current is assumed to be weak, i.e. $U_0 \ll C$. Stewart & Joy (1974) used a perturbation expansion in terms of a non-dimensional current speed parameter $\delta = U_0/C$ to demonstrate that the simple Doppler shift in the dispersion relation for uniform currents can be extended to arbitrary currents by using a weighted integral of the current over the depth if $\delta \ll 1$, i.e.

$$C = C_r + \tilde{U}, \tag{4.17}$$

where C_r is the linear phase speed relative to the currents,

$$C_r = \sqrt{\frac{g}{k}\tanh kh}, \tag{4.18}$$

and $\tilde{U}$ is a weighted-average current over the depth or equivalent uniform current. Stewart & Joy's (1974) formulation for deep water was later extended to finite water depth by Skop (1987) and Kirby & Chen (1989) and yields the following expression for the weighted-average current, $\tilde{U}$, in water of finite depth:

$$\tilde{U} = \frac{2k}{\sinh 2kh}\int_{-h}^{0} U(z)\cosh 2k(z+h)\,\mathrm{d}z. \tag{4.19}$$

A different form of Kirby & Chen's (1989) weighted-average dispersion relation can be obtained by substituting (4.18) and (4.19) into (4.17) and integrating by parts twice, resulting in

$$C = C_r + U_0 - \frac{U_0'}{2k}\tanh kh + \frac{1}{2k}\int_{-h}^{0} U''(z)\frac{\cosh 2k(z+h)}{\sinh 2kh}\,\mathrm{d}z. \tag{4.20}$$

The foregoing expression can also be recovered from the dispersion relation of the present boundary-integral formulation (4.16) by making several simplifying assumptions. If $U_0/C \ll 1$, we can replace $U - C$ in the denominator of the integral

https://doi.org/10.1017/S0022112009005850 Published online by Cambridge University Press

with $U_0 - C$, leading to the following approximate solution to (4.16):

$$C = U_0 - \frac{U_0'}{2k}\tanh kh + \frac{1}{2k}\int_{-h}^{0} U''(z)\frac{\cosh 2k(z+h)}{\sinh 2kh}\,\mathrm{d}z \pm \sqrt{\left(\frac{1}{2k}\int_{-h}^{0} U''(z)\frac{\cosh 2k(z+h)}{\sinh 2kh}dz - \frac{U_0'}{2k}\tanh kh\right)^2 + C_r^2}. \quad (4.21)$$

Equation (4.21) reduces to (4.20) if the mean flow vorticity (U_0') is much smaller than a characteristic wave frequency ($C_r k$), and the non-dimensional mean flow vorticity gradient (U_0'') is much smaller than the product of the characteristic wave frequency and wavenumber ($C_r k^2$).

5. Numerical solution

A numerical scheme has been developed to solve the one-dimensional form of the evolution equations for finite-amplitude waves propagating over an arbitrary current profile. The one-dimensional equations for the evolution of the free-surface elevation and tangential velocity at the free surface are given by

$$\eta_t \;=\; u_n - (U_\eta \eta)_x, \quad (5.1)$$

$$u_{s,t} + \left[g\,\eta + \frac{1}{2}u_s^2 - \frac{1}{2}\frac{(u_n + u_s\eta_x)^2}{(1+\eta_x^2)} + U_\eta u_s\right]_x + w_\eta\, U'|_\eta + \frac{1}{\rho}p_{g,x} + \mu(x)\,u_s = 0, \quad (5.2)$$

where $p_g(x)$ is a pressure distribution that is applied on the free surface to generate waves, while $\mu(x)$ is a quadratically varying Rayleigh damping coefficient that is used to absorb waves propagating out of the computational domain (e.g. Baker, Meiron & Orszag 1989; Wei, Kirby & Sinha 1999; Clamond *et al.* 2005). The evolution equations (5.1) and (5.2) have been recast in conservative form to allow for slow horizontal variations of depth-uniform current fields with vertical upwelling or downwelling ($W_\eta = \eta U_{\eta,x}$) to compensate for horizontal variations.

The computational domain is discretized into N segments in the horizontal direction. The evolution variables are defined in a staggered manner with the free-surface elevation and normal velocity defined at the mid-point of the segments, while the tangential velocities are defined at the edges of segments. A Gaussian-shaped pressure distribution is used to generate periodic waves inside the computational domain. The wavemaker is represented by

$$p_g(x,t) = p_0 \exp\left[-(x - x_g)^2/2\beta^2\right]\cos(\omega t), \quad (5.3)$$

where p_0 is the amplitude of the pressure distribution at its mid-point $x = x_g$; ω is the wave frequency; and β is a parameter related to the width of wavemaker. To generate waves of a given height, H, the amplitude of the pressure distribution is obtained by equating the average work done by the pressure distribution over a wave cycle to the energy flux of the radiated waves in the far field (e.g. Wehausen & Laitone 1960, § 21):

$$p_0 = \rho g \frac{H}{2}\frac{\mathrm{e}^{\frac{\beta^2 k^2}{2}}}{\beta k\sqrt{2\pi}}\left[1 + \frac{2kh}{\sinh 2kh}\right]. \quad (5.4)$$

https://doi.org/10.1017/S0022112009005850 Published online by Cambridge University Press

To maximize the rate at which the applied pressure transfers energy to the fluid, the pressure distribution is applied over one wavelength with $\beta = 1/k$ (Clamond *et al.* 2005).

The normal velocity of the free surface that is required to close the system of evolution equations is given by (3.13) and requires knowledge of the vorticity field $\Omega(x', z')$. The vorticity field can, in general, be obtained by solving the two-dimensional vorticity transport equation (2.27):

$$\Omega_t + (u + U)\,\Omega_x + w\Omega_z = -wU''. \tag{5.5}$$

This requires discretizing the water column into vertical layers and solving the transport equation for the evolution of the vorticity in each layer. The computational expense of multi-layer vorticity calculations would be similar to solving the full two-dimensional vertical plane Euler equations. To reduce the computational effort required to evaluate the vorticity field, we make several simplifying assumptions. Similar to the Rayleigh equation, we assume that the transport of vorticity by the perturbation wave velocity field (u, w) is much smaller than that due to the mean flow field U. We thus ignore the redistribution of vorticity in the vertical direction, since the unsteady (Ω_t) and horizontal advection terms $[(u + U)\partial\Omega/\partial x]$ will dominate the vertical advection term $[w\partial\Omega/\partial z]$.

We define a new parameter $\Lambda = \Omega/U''$ which is the ratio of the wave-induced vorticity to the mean flow vorticity gradient. Since vorticity is produced locally at each depth in proportion to the product of $w(z)$ and $U''(z)$, the vertical profile of $\Lambda(z)$ can be approximated by the vertical profile of the orbital wave velocity field $w(z)$. Hence, a single transport equation can be solved for the evolution of the free-surface value of Λ from which the entire vorticity field is reconstructed:

$$\Lambda_{\eta,t} + (u_\eta + U_\eta)\,\Lambda_{\eta,x} = -w_\eta. \tag{5.6}$$

Equation (5.6) is identical to the kinematic free-surface boundary condition (2.5) with the sign of the vertical velocity term reversed. The surface value of the vorticity parameter can thus be directly obtained from the free-surface elevation without having to solve the vorticity transport equation, i.e.

$$\Lambda_\eta = -\eta. \tag{5.7}$$

The vorticity field $\Omega = \Lambda U''$ is then explicitly determined from the product of the free-surface elevation and mean-flow vorticity gradient with its Fourier transform given as

$$\hat{\Omega}(k, z) = -\left[\frac{\mathrm{e}^{kz} - \mathrm{e}^{-k(z+2h)}}{1 - \mathrm{e}^{-2kh}}\right]\hat{\eta}(k)U''(z). \tag{5.8}$$

This is formally equivalent to using the kinematic free-surface boundary condition to replace the singular term on the right-hand side of the Rayleigh equation (4.2), i.e.

$$\frac{\hat{w}(k, z)}{U(z) - C} \approx \mathrm{i}k\left[\frac{\mathrm{e}^{kz} - \mathrm{e}^{-k(z+2h)}}{1 - \mathrm{e}^{-2kh}}\right]\hat{\eta}(k). \tag{5.9}$$

This approximation is consistent with the assumption made in deriving the linear dispersion relation (4.21) for arbitrarily sheared currents, i.e. $U(z) - C \approx U_0 - C$ if $U_0/C \ll 1$, and allows us to avoid the additional computational expense of numerically solving the two-dimensional vorticity transport equation.

The boundary-integral equation (3.13) is solved at every time step for the normal velocity. Since it is a Fredholm integral equation of the second kind with a diagonally

https://doi.org/10.1017/S0022112009005850 Published online by Cambridge University Press

dominant structure, we efficiently solve it using an iterative Neumann method without setting up and inverting a matrix. This contrasts with the Fredholm integral equation of the first kind that results from the standard boundary-integral formulation in terms of the velocity potential (e.g. Longuet-Higgins & Cokelet 1976). The first-kind integral equation leads to a dense and ill-conditioned matrix that is computationally expensive to invert. Direct evaluation of the convolution integrals in (3.13) still requires $O(N^2)$ operations per time step which is inefficient for long-term numerical simulations. The FFT technique can be used to speed up evaluation of convolution integrals and reduce the number of operations per time step to $O(N \log N)$. However, the FFT technique cannot be directly applied to the nonlinear integral operators in (3.13) due to the presence of the free-surface elevation $\eta(x')$ in the denominator of the kernel of the integral equation.

Two Fourier-based methods have been proposed for evaluating convolution integrals when the kernel is dependent on the interface or free-surface location. The first approach involves mapping the interface or free surface onto a flat plane and performing FFT operations in the mapped plane (e.g. Zakharov, Dyachenko & Vasilyev 2002; Hou, Hu & Zhang 2003). The second approach introduced by Clamond & Grue (2001) is a variant of the Ewald summation technique used in electrostatics. The integral operators are rewritten as a sum of far-field and near-field components with the kernel of the near-field component decaying more rapidly in physical space. The far-field (global) contributions to the convolution integrals are evaluated using the FFT method, while the near-field (local) contributions are directly evaluated over a limited region in physical space. A closely related approach is the asymptotic expansion method of Craig & Sulem (1993) where the linear integral operator is generalized to nonlinear surfaces and expanded as a Taylor series in η.

We adopt the approach of Clamond & Grue (2001) and introduce the parameters $D^2 = (\eta - \eta')^2/(x - x')^2$ for the kernels related to the free-space Green's function and $\tilde{D}^2 = [(\eta + \eta')^2 + 4h(\eta + \eta')]/[(x - x')^2 + 4h^2]$ for the kernels related to the image Green's function. As $x \to x'$, $D \to \eta_x$ and $\tilde{D} \to \sqrt{3}\,\eta/h$. Thus, D and $\tilde{D}$ respectively represent deep- and shallow-water wave steepness parameters. As shown in Appendix B, the kernels of the integral equation (3.13) can be expanded as a power series in D (or $\tilde{D}$) with an explicit remainder term:

$$K(x, x') = K_l(x, x')\frac{1}{1 + D^2} = K_l(x, x')\left[1 - D^2 + \frac{D^4}{1 + D^2}\right]. \tag{5.10}$$

Since both D and $\tilde{D}$ decay like $|x - x'|^{-1}$ as $|x - x'| \to \infty$, terms involving higher orders of D (or $\tilde{D}$) decay more rapidly in physical space. The decomposition in (5.10) can thus be used to separate the convolution integrals into far-field terms that decay slowly in space and near-field terms that decay rapidly in space. The FFT method is used to evaluate the leading-order contributions to the convolution integrals. Retention of terms up to $O(D^2)$ in the far-field integral ensures that the dominant four-wave interaction terms in deep water are evaluated using the accurate FFT method. We note that the remainder terms which decay like $|x - x'|^{-4}$ and higher are strongly singular and would require special numerical treatment. Although staggered positioning of the variables with the tangential velocities defined half a grid cell away from the normal velocity and free-surface elevation effectively regularizes the hyper-singular integrals, accurate evaluation of the integrals still requires a higher order numerical integration scheme. Hence, the remainder terms that would have rendered the model fully nonlinear have been ignored in the present computations.

https://doi.org/10.1017/S0022112009005850 Published online by Cambridge University Press

Starting from initially calm conditions, the fourth-order Runge–Kutta scheme is used to integrate (5.1) and (5.2) for the evolution of the free-surface elevation and tangential velocity at the free surface. The FFT-accelerated iterative Neumann scheme described in Appendix B is then used to invert (3.13) for the normal velocity. To minimize aliasing effects associated with performing FFT operations on nonlinear terms, the following low-pass anti-aliasing filter is applied to η and u_s at every time step:

$$f(k) = \exp\left[-2\pi(k/k_N)^{2m}\right], \tag{5.11}$$

where k_N is the Nyquist or maximum wavenumber and m is the order of the filter. We utilized $m = 10$ for most of the simulations presented in this paper. For $m = 10$, the value of $f(k)$ essentially remains constant at 1.0 through $k/k_N = 0.75$ before smoothly decreasing to zero at $k = k_N$.

6. Numerical results

The dispersive properties of the numerical model are initially investigated for finite-amplitude waves propagating over depth-uniform currents in deep water. Numerical model predictions of the phase speed and current-induced changes to the wave height are compared with analytical predictions. The numerical model is then used to investigate the modulational instability of deep-water gravity waves in vertically sheared current fields.

6.1. *Finite-amplitude wave propagation on uniform currents*

We simulate the propagation of two-dimensional periodic deep-water waves with frequency ω, height H_0, length $\lambda_0 = 2\pi/k_0$ and phase speed C_0 from calm water onto a region with steady depth-uniform currents, U. Numerical simulations were conducted for both small-amplitude waves with steepness $\varepsilon_0 = k_0 H_0/2 = 0.01$ and finite-amplitude waves with steepness $\varepsilon_0 = 0.2$, in both opposing currents and following currents over the range $-0.2 < U/C_0 < 1$. The computational domain was 32 wavelengths long. The simulations were performed with grid spacing $\Delta x = \lambda_0/32$ and time step size $\Delta t = T/50$. The magnitude of the current was ramped from zero to U over the distance $5\lambda_0 < x < 7\lambda_0$ from the centre of the pneumatic wavemaker using a cosine-bell transition window as shown in figure 2.

A snapshot of the instantaneous free-surface elevation is shown in figure 2 for the test condition with $\varepsilon_0 = 0.01$ and $U/C_0 = 1$. As expected, the height of the wave decreased, while its length increased, since the waves were propagating in the same direction as the currents. The wave height in this case decreased to about 40 % of the incident wave height, while the wavelength increased by approximately 160 %. The numerical results were analysed to obtain estimates of the phase speed and wave height for comparisons with analytical predictions. The phase speed was obtained from a cross-correlation analysis of the surface elevation time histories at two locations a quarter of a wavelength apart, while the wave heights were obtained from a zero-crossing analysis of the time records. The analytical predictions are based on theories presented by Longuet-Higgins & Stewart (1961) for small-amplitude waves and Peregrine & Thomas (1979) for finite-amplitude waves. For small-amplitude waves, the phase speed relative to the currents is given by (4.17) and (4.18) as

$$C_r^2 = (C - U)^2 = \frac{g}{k}, \tag{6.1}$$

https://doi.org/10.1017/S0022112009005850 Published online by Cambridge University Press

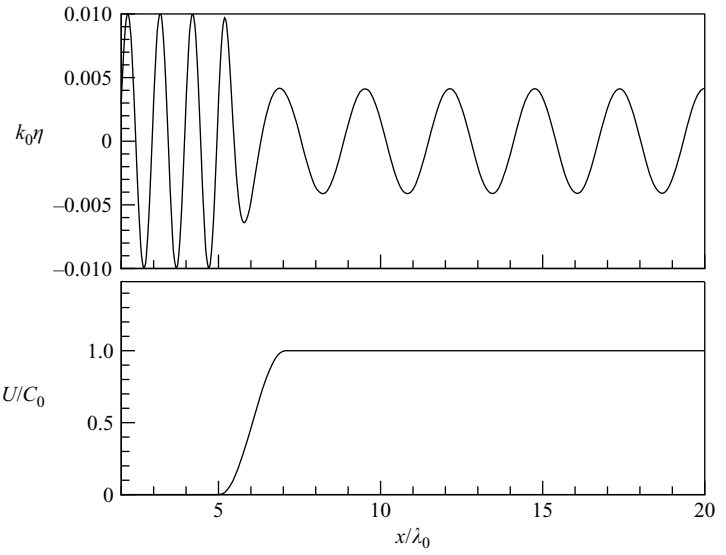


FIGURE 2. Spatial profile of small-amplitude wave ($\varepsilon_0 = 0.01$) propagating onto a uniform current ($U/C_0 = 1$).

where C represents the phase speed relative to a fixed frame of reference. Replacing the wavenumber k with ω/C, (6.1) can be solved to obtain an explicit expression for the non-dimensional phase speed in terms of the non-dimensional current speed:

$$\frac{C}{C_0} = \frac{U}{C_0} + \frac{1}{2}\left(1 + \sqrt{1 + 4\frac{U}{C_0}}\right), \tag{6.2}$$

where $C_0 = g/\omega$. Changes to the wave height H due to the presence of the current is given by Longuet-Higgins & Stewart (1961) as

$$\frac{H}{H_0} = \left[\frac{C_0^2}{C_r\,(C_r + 2U)}\right]^{1/2}. \tag{6.3}$$

The foregoing expression is valid for small-amplitude waves. For finite-amplitude waves, the averaged Lagrangian method of Whitham (1965) is often used to determine the change in wave height. Crapper (1972) employed an approximate Lagrangian based on the first two terms of an asymptotic series expansion. A more accurate expression for the averaged Lagrangian was derived by Peregrine & Thomas (1979) using rational function approximations of Longuet-Higgin's (1975) solutions for the integral properties of steep waves up to the limiting wave height. It yields the following wave action conservation equation for finite-amplitude waves:

$$\frac{\rho g}{k^3}\left[(E + 5L) + \frac{2U}{C_r}(E + L)\right] = \text{ constant}, \tag{6.4}$$

where $E(\varepsilon)$ and $L(\varepsilon)$ are respectively non-dimensional rational function approximations of the averaged wave energy density and Lagrangian,

$$E(\varepsilon) = \frac{1}{2}\varepsilon^2 - \frac{0.19569\varepsilon^4}{1 - 1.04488\varepsilon^2 - 12.9792\varepsilon^4}, \tag{6.5}$$

$$L(\varepsilon) = \frac{1}{8}\varepsilon^4 - \frac{0.007157\varepsilon^6}{1 - 6.73868\varepsilon^2 + 9.64103\varepsilon^4}. \tag{6.6}$$

https://doi.org/10.1017/S0022112009005850 Published online by Cambridge University Press

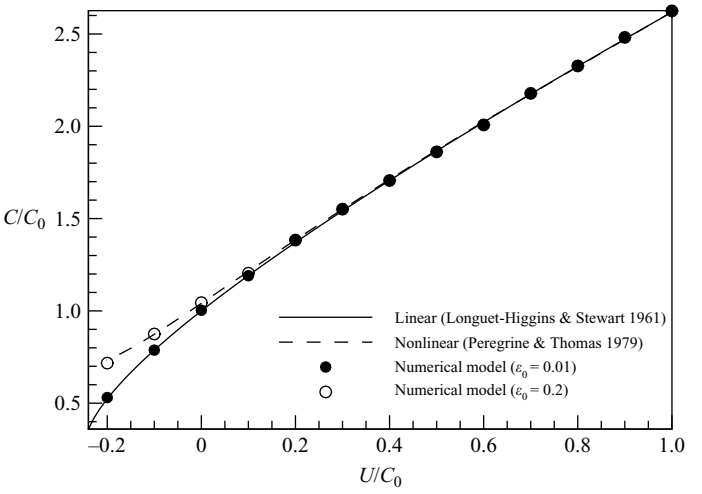


FIGURE 3. Variation of phase speed with relative current magnitude for small-amplitude and finite-amplitude waves in depth-uniform currents.

We note that (6.4) reduces to (6.3) at $O(\varepsilon^2)$. The wave action conservation equation involves four interdependent variables: k, C_r, U and ε. Peregrine & Thomas (1979) used the Doppler-shifted frequency relation

$$\omega = k(C_r + U) \tag{6.7}$$

and nonlinear dispersion relation

$$C_r^2 = \frac{g}{k} S(\varepsilon) = \frac{g}{k}\left[1 + \varepsilon^2 + \frac{2.6107\varepsilon^4(0.1935 - \varepsilon^2)}{1 - 5.63543\varepsilon^2 + 3.98484\varepsilon^4}\right] \tag{6.8}$$

to eliminate k and U from (6.4), yielding a seventh-order polynomial for C_r:

$$\frac{2\omega}{g^4 S^4}(E + L)\, C_r^7 - \frac{1}{g^3 S^3}(E - 3L)\, C_r^6 = \frac{1}{k_0^3}(E(\varepsilon_0) + 5L(\varepsilon_0)). \tag{6.9}$$

Given an incident wave with wavenumber k_0 and steepness ε_0 in the absence of currents, (6.9) is solved to determine C_r at different values of ε. The corresponding wavenumber is then determined from (6.8), while the current speed is determined from (6.7).

The numerically predicted phase speeds are compared with the theoretical results in figure 3. For small-amplitude waves with $\varepsilon_0 = 0.01$, the numerical model accurately predicts the phase speed over the entire range $-0.2 < U/C_0 < 1$. The phase speed for finite-amplitude waves starts to significantly deviate from the linear solution for $U/C_0 < 0.1$. This is due to the increase in phase speed with increasing wave steepness as predicted by (6.8). Since the wave steepness increases in opposing currents and decreases in following currents, the effect is more pronounced for opposing currents. The nonlinear wave model is able to predict the observed trend for finite-amplitude waves and match the theoretical model of Peregrine & Thomas (1979) reasonably well.

Current-induced changes to the wave height are plotted as functions of non-dimensional current speed in figure 4. In following currents, the wave heights for finite-amplitude waves are marginally larger than their small-amplitude counterpart. The nonlinear wave model accurately predicts the slight increase in wave height. In opposing currents ($U < 0$), the wave height amplification factor for finite-amplitude waves ($\varepsilon_0 = 0.2$) increases at a much slower rate than predicted by the small-amplitude

https://doi.org/10.1017/S0022112009005850 Published online by Cambridge University Press

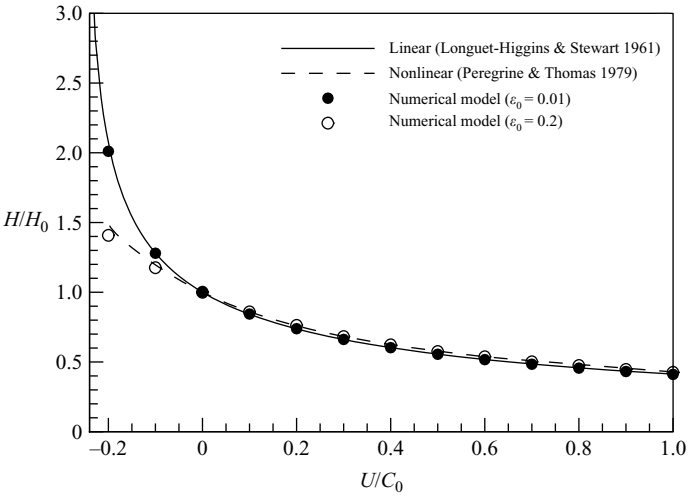


FIGURE 4. Variation of wave height with relative current magnitude for small-amplitude and finite-amplitude waves in depth-uniform currents.

theory of Longuet-Higgins & Stewart (1961). The waves also break prior to the critical current speed, $U = -0.25C_0$. The Peregrine–Thomas model predicts wave breaking at $U/C_0 \approx -0.2$, when the wave steepness reaches the limiting value of 0.44. The present numerical solution became unstable at $U/C_0 \approx -0.2$ at a slightly lower steepness of 0.39. One would however expect slight differences between the different nonlinear models in the vicinity of the limiting wave steepness, since the Peregrine–Thomas model used rational functions to approximate the Lagrangian up to $\varepsilon = 0.44$, while the present model is based on a third-order expansion of the boundary-integral closure relationship.

6.2. *Modulational instability of deep-water waves*

The Benjamin–Feir instability mechanism (Benjamin & Feir 1967) has been hypothesized to be one of the causes of rogue waves or extremely large waves that tend to appear out of nowhere in relatively calm seas (e.g. Kharif & Pelinovsky 2003; Dysthe, Krogstad & Muller 2008). Although numerous theoretical and experimental studies of the sideband instability phenomenon have been conducted, very few of those studies have considered vertically sheared currents which are a characteristic feature of wind-generated currents in the deep ocean. The present numerical method is used to investigate the modulational instability of finite-amplitude waves in vertically sheared current fields. We initially study the classical Benjamin–Feir instability mechanism in the absence of currents to validate the model and to also serve as a benchmark for the wave–current interaction studies.

6.2.1. *Waves without currents*

Numerical simulations were performed using an initial condition that consists of a small-amplitude carrier wave with amplitude a_c and wavenumber k_c and perturbations at wavenumbers $k_\pm = k_c \pm \Delta k$ slightly detuned from the carrier wavenumber:

$$\eta(x) = a_c \cos(k_c x) + a_- \cos[(k_c - \Delta k)x - \phi_-] + a_+ \cos[(k_c + \Delta k)x - \phi_+], \tag{6.10}$$

$$u_s(x) = \omega a_c \cos(k_c x) + \omega_- a_- \cos[(k_c - \Delta k)x - \phi_-] + \omega_+ a_+ \cos[(k_c + \Delta k)x - \phi_+]. \tag{6.11}$$

https://doi.org/10.1017/S0022112009005850 Published online by Cambridge University Press

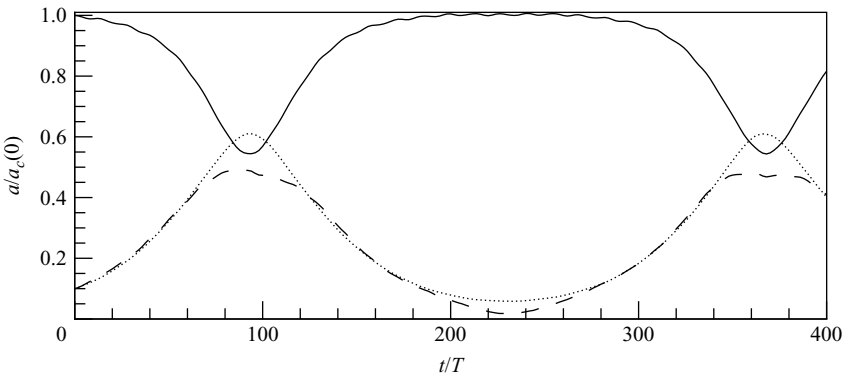


FIGURE 5. Time-dependent evolution of the Fourier amplitudes of the carrier wave (solid line) and lower (dotted line) and upper (dashed line) sidebands for a modulated wavetrain with initial steepness $\varepsilon = 0.1$.

The first numerical test was chosen to match one of the conditions in Landrini *et al.* (1998) who compared a fully nonlinear boundary-integral model with several weakly nonlinear formulations. To avoid wave breaking, we picked a moderately steep carrier wave with initial steepness $\varepsilon = a_c k_c = 0.1$. The initial amplitudes of the upper and lower sidebands $a_\pm$ were set equal to 10 % of the carrier wave amplitude. The perturbation wavenumbers and relative phase angles were selected to provide maximum initial growth based on the theory of Benjamin & Feir (1967) with $\Delta k = 0.2k_c$ and $\phi_\pm = \pi/4$. A computational domain containing 10 modulations (50 carrier wavelengths) with $N = 2048$ computational grid points was used. The simulations were carried out for a duration of 400 wave periods at time step size $\Delta t = T/80$.

The temporal evolution of the normalized Fourier amplitudes of the carrier wave and upper and lower sidebands are shown in figure 5. Strong nonlinear interactions between the carrier wave and sidebands lead to the transfer of energy from the carrier to sideband frequencies with the amplitudes of the sidebands growing exponentially in time. Initially, the amplitudes of the lower and upper sidebands grow at the same rate. As the peak of the first modulation cycle is approached, the lower sideband component grows larger than that of the upper sideband in contrast to the symmetric growth pattern predicted by Benjamin–Feir theory. The predicted asymmetries in the amplitudes of the sidebands at the peak of the modulation cycle are consistent with the fully nonlinear numerical model results of Landrini *et al.* (1998). The time scale for the occurrence of the first modulation peak ($t/T \approx 93$) also matches their results. For $t/T > 93$, the waves start to demodulate with reverse energy transfer from the sidebands to the carrier wave. The modulation and demodulation cycles recur with a period of $275T$ which is close to an estimated value of $278T$ from Landrini *et al.* (1998).

The free-surface profiles are plotted in figure 6 for the initial condition ($t/T = 0$), peak of first modulation cycle ($t/T = 93$) and minima of demodulation cycle ($t/T = 230$). The corresponding Fourier amplitude spectra are also shown in figure 6. At $t/T = 93$, the wavetrain has significantly evolved from the weakly modulated form at $t/T = 0$ to a wave packet with a distinct extreme wave at the centre of the group. The crest elevation of the large wave is about two and half times the initial amplitude of the carrier wave. The amplitude spectrum also changes from a narrowband one at $t/T = 0$ to a broadband continuous spectrum at $t/T = 93$. The broadband spectrum

https://doi.org/10.1017/S0022112009005850 Published online by Cambridge University Press

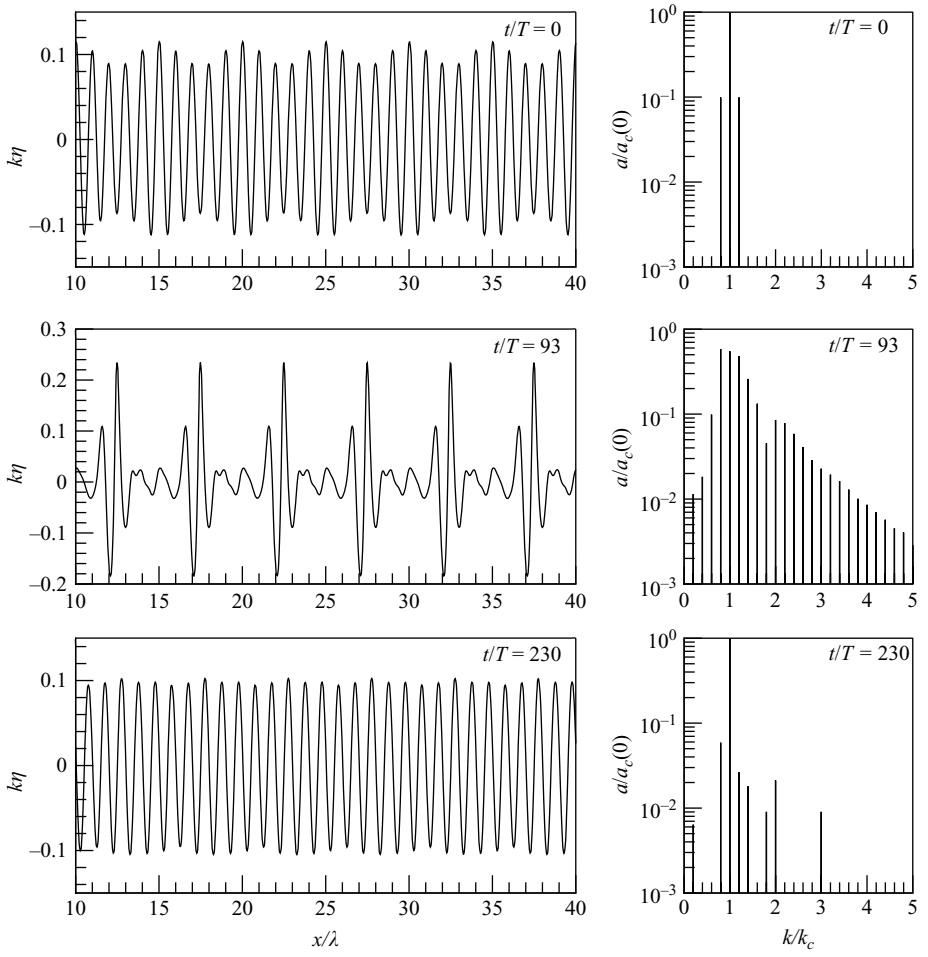


FIGURE 6. Spatial profiles of the free-surface elevation at $t/T = 0$, 93 and 230 and associated amplitude spectra for an evolving modulated wavetrain with initial steepness $\varepsilon = 0.1$.

is similar to wind-generated wave spectra and underscores the role of nonlinear wave–wave interactions in the evolution of wind-generated waves. At $t/T = 230$, the demodulated waves do not recover the exact initial conditions, as the amplitude of the lower sideband is larger than that of the upper sideband. Several other harmonics are also present that combine to make the demodulated wavetrain less modulated than the initial condition.

The average growth rate of the sidebands (γ) was estimated by fitting the following line $\ln[a_{\pm}(t)] = \ln[a_{\pm}(0)] + \gamma t$ to the early part of the time record in figure 5. The normalized growth rate is shown in figure 7 in addition to theoretical estimates of the growth rates from Crawford *et al.* (1981) and the Benjamin–Feir growth rate which is given by

$$\gamma = \frac{\omega}{\sqrt{8}} \frac{\Delta k}{k} \left[a^2 k^2 - \frac{1}{8} \left(\frac{\Delta k}{k} \right)^2 \right]^{1/2}. \tag{6.12}$$

The estimated growth rates from numerical simulations for other relative sideband widths ($\Delta k/k$) are also shown in figure 7. Excellent agreement is observed between

https://doi.org/10.1017/S0022112009005850 Published online by Cambridge University Press

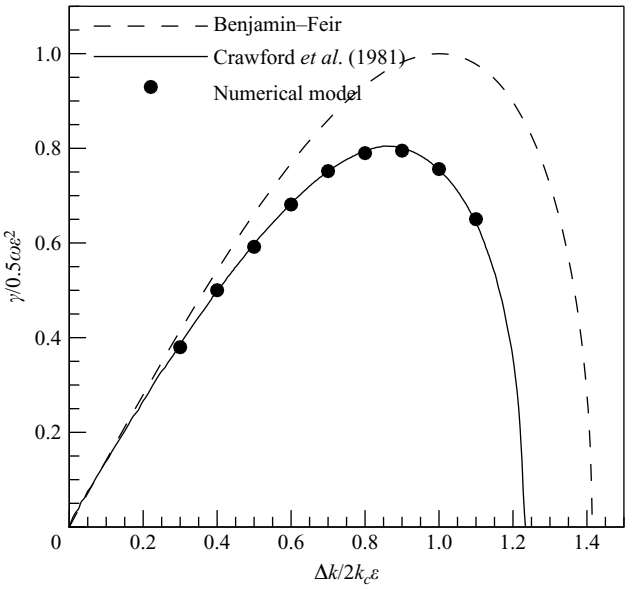


FIGURE 7. Comparison of the numerically and theoretically predicted sideband growth rates for a modulated wavetrain with initial steepness $\varepsilon = 0.1$.

the estimated growth rates from the present numerical model with the results of Crawford *et al.* (1981) who solved third-order form of the Zhakarov (1968) equation. The present FFT-accelerated boundary-integral model in which nonlinear terms up to the third order in wave steepness are evaluated in physical space can be considered to be equivalent to the Zhakarov model in which the third-order nonlinear terms are evaluated in wavenumber space. The Benjamin–Feir model overestimates the growth rate for this moderately steep wave ($\varepsilon = 0.1$) for large values of the non-dimensional perturbation wavenumber $\Delta k/2k_c\varepsilon$ but becomes asymptotically valid as $\Delta k/2k_c\varepsilon \to 0$.

6.2.2. *Depth-uniform currents*

The effect of depth-uniform currents on the Benjamin–Feir instability mechanism is relatively well established (e.g. Gerber 1987). The presence of a mean flow suppresses instability for waves propagating in the same direction as the currents and enhances instability for waves propagating against currents. There is however very little work on vertically sheared currents. Preliminary evidence from Li *et al.* (1988) using a linear shear current and Baumstein (1998) using a piecewise linear current suggests that weak velocity shear can enhance instability, while strong velocity shear can suppress instability. Numerical simulations were performed for both a depth-uniform current field and a more realistic exponentially sheared current profile in deep water. To model a situation analogous to waves propagating onto a current field in which the wavelength and hence steepness changes but the wavenumber separation remains the same, the initial conditions for the wave–current field were calculated using the same carrier wave amplitude and non-dimensional perturbation wavenumber as the wave-only simulations, i.e. $a_c(0) = \varepsilon/k_c = (\varepsilon/k_c)_0$ and $\Delta k/k_c = (\Delta k/k_c)_0$, where the subscript 0 is used to denote values of parameters in the absence of currents.

The time-dependent evolution of the carrier and sideband amplitudes in a depth-uniform current field with $a_c(0) = 0.1/k_0$, $a_{\pm}(0) = 0.1a_c(0)$ and $\Delta k/k = 0.2$ are shown in figure 8 for both a weak following current ($U/C_0 = 0.1$) and a weak opposing current

https://doi.org/10.1017/S0022112009005850 Published online by Cambridge University Press

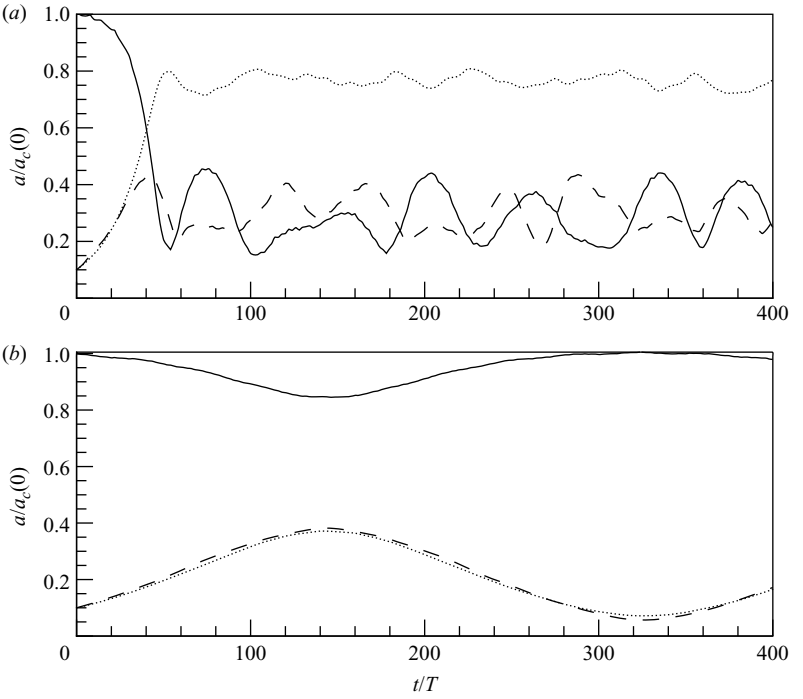


FIGURE 8. Time-dependent evolution of the Fourier amplitudes of the carrier wave (solid line) and lower (dotted line) and upper (dashed line) sidebands for a modulated wavetrain with initial steepness $\varepsilon_0 = 0.1$ in a depth-uniform current field: (*a*) $U/C_0 = -0.1$; (*b*) $U/C_0 = 0.1$.

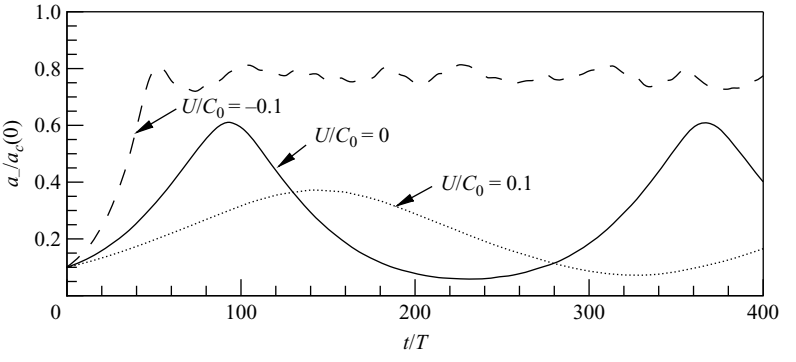


FIGURE 9. Comparison of the time-dependent evolution of the Fourier amplitudes of the lower sideband component for a modulated wavetrain with initial steepness $\varepsilon = 0.1$ for different non-dimensional current speeds.

($U/C_0 = -0.1$). The rate of growth of the sideband amplitudes in following currents is significantly reduced with the sidebands attaining much lower maximum amplitudes compared to the wave-only case. This can be seen more clearly in figure 9 in which the lower sideband amplitudes in the wave–current field are directly compared with the wave-only results. The decrease in the growth rate in the current field can be attributed to the decrease in the initial steepness of the waves in the wave–current

https://doi.org/10.1017/S0022112009005850 Published online by Cambridge University Press

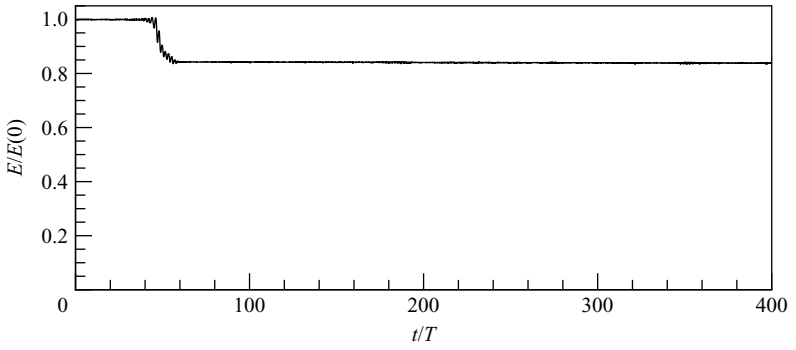


FIGURE 10. Time history of total energy in computational domain for modulated wavetrain with initial steepness $\varepsilon_0 = 0.1$ in depth-uniform current field with $U/C_0 = -0.1$.

field. For $U/C_0 = 0.1$, the wavenumber decreases by 16 %, resulting in a reduction of the initial steepness ε from 0.1 to 0.084.

The evolution of the Fourier amplitudes in opposing currents (figure 8*a*) shows a much more rapid growth of instability. The computations initially broke down at $t/T \approx 45$ when the amplitude of the lower sideband was approximately twice that of the upper sideband. The breakdown of the computations was attributed to wave breaking, since previous numerical studies (e.g. Banner & Tian 1998) have shown that modulated wavetrains with $\Delta k/k = 0.2$ break when the initial steepness $\varepsilon > 0.1125$. For $U/C_0 = 0.1$, the initial wave steepness $\varepsilon = 0.127$ which is greater than the breaking threshold of 0.1125. To stabilize the computations past the breaking point, the order of the anti-aliasing filter in (5.11) had to be decreased from $m = 10$ to $m = 6$, leading to artificial numerical dissipation of energy. We monitored the total energy over the computational domain:

$$E(t) = \frac{1}{2}\rho g \int_{-\infty}^{\infty} \eta^2 \mathrm{d}x + \frac{1}{2}\rho \int_{-\infty}^{\infty}\int_{-\infty}^{\eta} \left[(u+U)^2 + w^2\right] \mathrm{d}z\mathrm{d}x - \frac{1}{2}\rho \int_{-\infty}^{\infty}\int_{-\infty}^{0} U^2 \mathrm{d}z\mathrm{d}x. \tag{6.13}$$

The total energy is plotted as a function of time in figure 10. Energy was conserved to within 0.05 % of its initial value until $t/T \approx 30$ when it started to oscillate rapidly. At $t/T \approx 45$, the anti-aliasing filter started to extract energy from the system. The overall energy eventually decayed to a stable region of approximately 84 % of its initial value. The artificial energy dissipation led to the non-recurrence of the lower sideband amplitude observed in figure 9.

6.2.3. *Exponentially sheared currents*

We next consider the evolution of modulated wavetrains in exponentially sheared current fields. The current profile is defined up to the instantaneous free-surface elevation:

$$U(z) = U_0 \exp(z/d), \qquad -\infty < z < \eta, \tag{6.14}$$

where d is a characteristic current depth with the current decaying to 4 % of its surface value at $z = -\pi d$. Numerical simulations were initially conducted for small-amplitude periodic waves ($\varepsilon = 0.01$) without sidebands to ensure that the wave propagation speed in the numerical model was consistent with the linear dispersion relation. Figure 11 shows a comparison of the phase speeds obtained from the model for $k_0 d = 1$ with the theoretical relation (4.21) and the weighted-average formulation of Stewart & Joy (1974). The equivalent uniform current approach of Stewart & Joy (1974) gives

https://doi.org/10.1017/S0022112009005850 Published online by Cambridge University Press

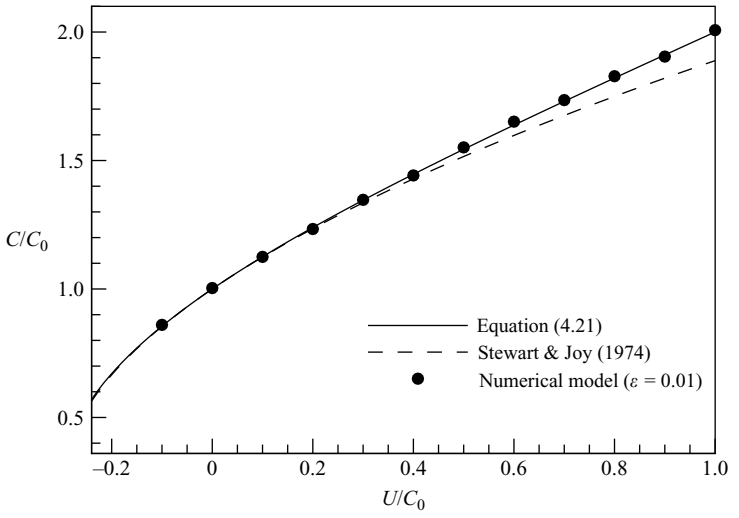


FIGURE 11. Variation of phase speed with relative current magnitude for an exponentially sheared current with $k_0 d = 1$.

reasonable predictions of the phase speed over the range $-0.25 < U/C_0 < 0.4$, although it is based on the assumption that $U/C_0 \ll 1$.

The modulational instability tests were repeated for the exponentially sheared current field with initial conditions $a_c(0) = 0.1/k_0$, $a_{\pm}(0) = 0.1a_c(0)$ and $\Delta k/k = 0.2$. The simulations were performed for three characteristic current depths $k_0 d = 1.5$, 1.0 and 0.5 corresponding to mean flow vorticities $U_0^{'}/\omega = 0.067$, 0.1 and 0.2 respectively. The surface value of the current was kept constant at $U_0/C_0 = 0.1$.

The time-dependent evolution of the Fourier amplitudes of the carrier and sideband components are shown in figure 12. For a given surface current speed, the sideband growth rate increases as the mean flow vorticity $U_0^{'}/\omega$ increases (or $k_0 d$ decreases). This is qualitatively consistent with the weighted-average or equivalent uniform current decreasing as the characteristic current depth $k_0 d$ decreases. However, the growth rate in a sheared current field can be larger than predicted using an equivalent uniform current. The evolutions of the lower sideband amplitudes for the three characteristic current depths are directly compared to the wave-only case in figure 13. Although the waves are propagating in the same direction as the currents, the growth rate of extreme waves is enhanced relative to the without current case when $k_0 d$ becomes smaller than ~ 1. The equivalent uniform current approach, however, always predict a suppression of instability for following currents. Hence, the Stewart & Joy (1974) equivalent-uniform current approach cannot be used to predict the dynamics of nonlinear interaction in strongly sheared currents, although it might accurately predict the linear phase speed.

The present results also appear to contradict the findings of Li *et al.* (1987) and Baumstein (1998) who found instability was enhanced at small vorticity values but suppressed at larger vorticities. We note that Baumstein (1998) used a current profile that linearly decreased from its surface value to zero at a specified depth. Increases in the mean flow vorticity were thus directly correlated with increases in the surface current speed. It is however useful to separate the influences of the surface current U_0/C_0 and surface vorticity $U_0^{'}/\omega$, given the complex interplay between the two parameters. For a given U_0/C_0, the mean flow vorticity will always act to enhance

https://doi.org/10.1017/S0022112009005850 Published online by Cambridge University Press

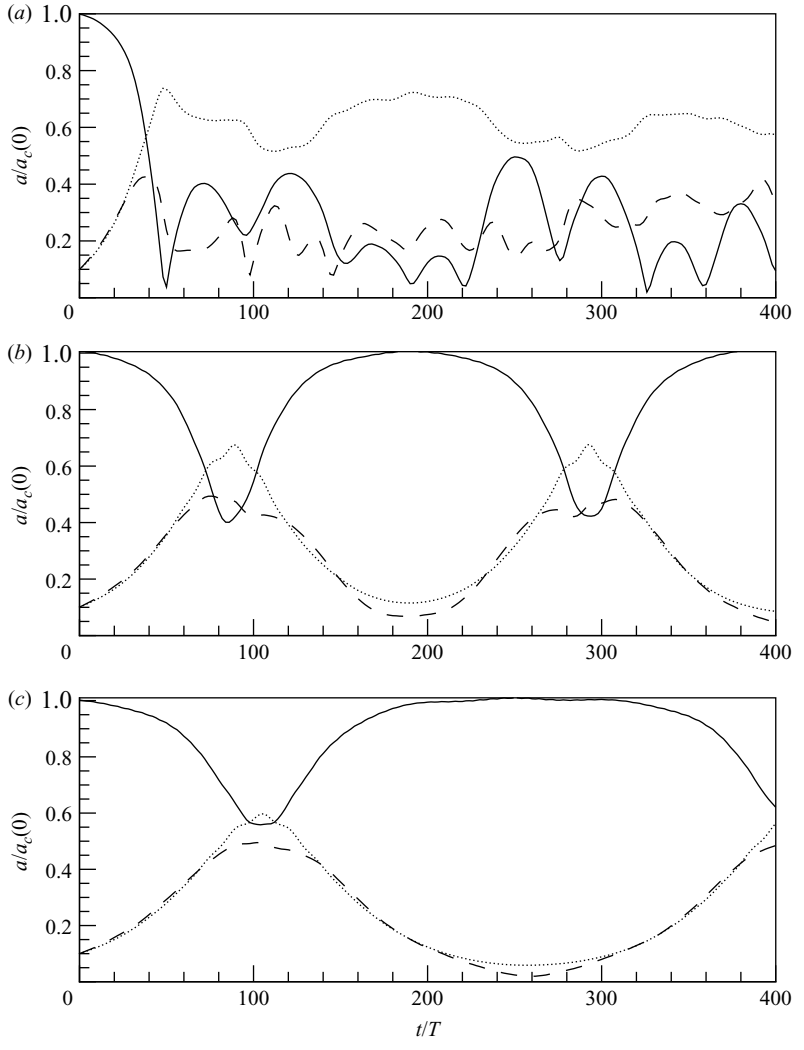


FIGURE 12. Time-dependent evolution of the Fourier amplitudes of the carrier wave (solid line) and lower (dotted line) and upper (dashed line) sidebands for a modulated wavetrain with initial steepness $\varepsilon_0 = 0.1$ in an exponentially sheared current field: (*a*) $k_0 d = 0.5$; (*b*) $k_0 d = 1.0$; (*c*) $k_0 d = 1.5$.

instability. However, the instability will eventually be suppressed for relatively strong currents.

We note that the representation of the current field in the near-surface region could be critical to the dynamics of nonlinear wave–wave interaction in strongly sheared current fields. A vertically sheared current profile that is defined up to $z = 0$ in the absence of waves could be significantly distorted in near-surface region in the presence of waves and differ from the approximation we adopted in (6.14). In addition, the overall current profile could change as has been observed in laboratory experiments (e.g. Swan, Cummins & James 2001). We have not considered changes to the mean current field in the present study. Viscous effects due to turbulent fluctuations in the

https://doi.org/10.1017/S0022112009005850 Published online by Cambridge University Press

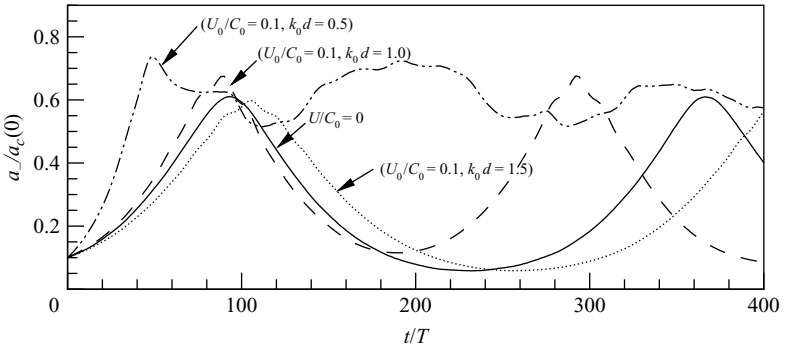


FIGURE 13. Comparison of the time-dependent evolution of the Fourier amplitudes of the lower sideband component for a modulated wavetrain with initial steepness $\varepsilon_0 = 0.1$ in vertically sheared current fields with the wave-only results.

current field could play an important role in the momentum exchange process and are considered beyond the scope of this paper.

7. Concluding remarks

A novel numerical method has been developed to simulate the interaction of steep gravity waves with vertically sheared currents. The vector form of Green's second identity was used to derive a closure scheme that is consistent with decomposing the velocity field into rotational and irrotational components. The irrotational component is obtained from a boundary integral of a mixed distribution of sources and vortices, while the rotational component is obtained from the Biot–Savart law. The closure relationship leads to strongly singular integrals that are computational expensive to invert. For non-overturning waves, the kernels of the boundary integrals were expanded in powers of the wave steepness parameter proposed by Clamond & Grue (2001). An FFT-based scheme was then used to accurately evaluate the strongly singular integrals. The FFT technique avoids some of the pitfalls of direct numerical integration of strongly singular integrals and reduces the number of operations on N computational grid points from $O(N^2)$ to $O(N\log N)$, making the numerical scheme efficient for long-term simulations of evolving nonlinear wave fields.

The linear dispersive properties of the system of equations for wave–current fields were derived from the Fourier transform of the evolution equations and closure relationship and shown to be consistent with the analytical expressions of Thompson (1949) for linear shear currents and Stewart & Joy (1974) for arbitrary current profiles. The numerical model was then used to investigate nonlinear wave–current interaction in depth-uniform current fields. Changes to the wave height and phase speed were compared to analytical predictions by Longuet-Higgins & Stewart (1961) for small-amplitude waves and Peregrine & Thomas (1979) for finite-amplitude waves. Differences between the linear and nonlinear solutions were most pronounced for waves travelling in a direction opposite to the currents. The increase in wave steepness led to an increase in the phase speed and a decrease in the wave height amplification factor. Excellent agreement was observed between the numerical model results and the theoretical model of Peregrine & Thomas (1979).

We also investigated the modulational instability of deep-water waves in both depth-uniform and exponentially sheared current fields. The presence of a depth-uniform

https://doi.org/10.1017/S0022112009005850 Published online by Cambridge University Press

mean flow was found to suppress instability for waves propagating in the same direction as the currents and enhance instability for waves propagating against currents. However, in vertically sheared current fields, the mean flow vorticity acted to enhance instability in following currents relative to the wave-only case. This could have significant implications in developing a better understanding of the dynamics of rogue waves in the deep ocean in which strongly sheared currents often exist near the sea surface even under light wind conditions.

While the focus of this paper has been on nonlinear wave interaction with currents, the velocity-based boundary/volume integral approach is quite general and can be applied to free-surface flow problems with an arbitrary distribution of vortices below the free surface, provided the initial distribution of vorticity and/or time-dependent vorticity generation terms are well defined.

This research was supported by the Multidisciplinary University Research Initiative (MURI) program of the Office of Naval Research through Contract Number N00014-05-1-0537 to the University of Michigan with Dr C. Linwood Vincent and Dr P. Purtell as program managers.

Appendix A. Derivation of Biot–Savart integral

The velocity field associated with the vorticity distribution is given by the vector form of Green's second identity (3.8) as

$$\boldsymbol{U}_{\Omega}(\boldsymbol{x}) = -\int\int_{V}\int G(\boldsymbol{x};\boldsymbol{x}')\,[\nabla'\times\boldsymbol{\Omega}(\boldsymbol{x}')]\,\mathrm{d}V - \oint_{\partial V} G(\boldsymbol{x};\boldsymbol{x}')\,[\boldsymbol{\Omega}(\boldsymbol{x}')\times\boldsymbol{n}(\boldsymbol{x}')]\,\mathrm{d}S. \quad (\mathrm{A}\,1)$$

The foregoing equation can also be rewritten in the more familiar Biot–Savart form. The vector product rule $\nabla\times(G\boldsymbol{\Omega}) = G(\nabla\times\boldsymbol{\Omega}) - \boldsymbol{\Omega}\times\nabla G$ is initially used to rewrite the volume integral in (A1):

$$\boldsymbol{U}_{\Omega}(\boldsymbol{x}) = -\int\int_{V}\int \boldsymbol{\Omega}\times\nabla G\,\mathrm{d}V - \int\int_{V}\int \nabla\times(G\boldsymbol{\Omega})\,\mathrm{d}V - \oint_{\partial V} G\,[\boldsymbol{\Omega}\times\boldsymbol{n}]\,\mathrm{d}S. \quad (\mathrm{A}\,2)$$

The first term on the right-hand side of (A 2) corresponds to the Biot–Savart integral. The second volume integral on the right hand side of (A 2) can be converted to a boundary integral using the divergence theorem. Taking the dot product of the second volume integral with the unit vector $\boldsymbol{e}_j$ in the jth coordinate direction and making use of the vector identity $\nabla\cdot(\boldsymbol{A}\times\boldsymbol{B}) = \boldsymbol{B}\cdot(\nabla\times\boldsymbol{A}) - \boldsymbol{A}\cdot(\nabla\times\boldsymbol{B})$, we obtain

$$\int\int_{V}\int \boldsymbol{e}_j\cdot[\nabla\times(G\boldsymbol{\Omega})]\,\mathrm{d}V = -\int\int_{V}\int \nabla\cdot(\boldsymbol{e}_j\times G\boldsymbol{\Omega})\,\mathrm{d}V, \quad (\mathrm{A}\,3)$$

since $\nabla\times\boldsymbol{e}_j = 0$. The divergence theorem is then used to convert the volume integral on the right-hand side of (A 3) to a surface integral:

$$\int\int_{V}\int \boldsymbol{e}_j\cdot[\nabla\times(G\boldsymbol{\Omega})]\,\mathrm{d}V = -\oint_{\partial V}(\boldsymbol{e}_j\times G\boldsymbol{\Omega})\cdot\boldsymbol{n}\,\mathrm{d}S. \quad (\mathrm{A}\,4)$$

We further use the vector identity $\boldsymbol{A}\cdot(\boldsymbol{B}\times\boldsymbol{C}) = (\boldsymbol{A}\times\boldsymbol{B})\cdot\boldsymbol{C}$ to rewrite (A 4) as

$$\int\int_{V}\int \boldsymbol{e}_j\cdot[\nabla\times(G\boldsymbol{\Omega})]\,\mathrm{d}V = -\oint_{\partial V}\boldsymbol{e}_j\cdot(G\boldsymbol{\Omega}\times\boldsymbol{n})\,\mathrm{d}S. \quad (\mathrm{A}\,5)$$

https://doi.org/10.1017/S0022112009005850 Published online by Cambridge University Press

Since $\boldsymbol{e}_j$ is arbitrary, (A 5) reduces to a three-dimensional variant of Stokes theorem:

$$\int\int_V\int \nabla\times(G\boldsymbol{\Omega})\,\mathrm{d}V \;\; = -\oint_{\partial V} G\,(\boldsymbol{\Omega}\times\boldsymbol{n})\,\mathrm{d}S. \tag{A 6}$$

Substituting (A 6) into (A 2), we finally obtain the Biot–Savart form of the equations:

$$\boldsymbol{U}_{\Omega}(\boldsymbol{x}) = -\int\int_V\int \boldsymbol{\Omega}\times\nabla G\;\mathrm{d}V. \tag{A 7}$$

Appendix B. FFT-based iterative solver for closure equation

The closure relationship (3.13) that is used to determine the normal velocity of the free surface, u_n, from the tangential velocity at the free surface, u_s, free-surface elevation, η, and vorticity field, Ω, can be rewritten as a set of integral operators:

$$u_n - \mathscr{L}^{(1)}[u_n] = \mathscr{L}^{(2)}[u_s] + \mathscr{L}^{(3)}[\Omega], \tag{B 1}$$

where

$$\mathscr{L}^{(1)}[f] = \frac{1}{\pi}\int_{-\infty}^{\infty}\left\{\frac{[(x-x')\eta_x - (\eta-\eta')]}{[(x-x')^2+(\eta-\eta')^2]} + \frac{[(x-x')\eta_x - (2h+\eta+\eta')]}{[(x-x')^2+(2h+\eta+\eta')^2]}\right\} f(x')\,\mathrm{d}x', \tag{B 2}$$

$$\mathscr{L}^{(2)}[f] = \frac{1}{\pi}\int_{-\infty}^{\infty}\left\{\frac{[(x-x') + (\eta-\eta')\eta_x]}{[(x-x')^2+(\eta-\eta')^2]} - \frac{[(x-x') + (2h+\eta+\eta')\eta_x]}{[(x-x')^2+(2h+\eta+\eta')^2]}\right\} f(x')\,\mathrm{d}x', \tag{B 3}$$

$$\mathscr{L}^{(3)}[f] = -\frac{1}{\pi}\int_{-h}^{\eta'}\int_{-\infty}^{\infty}\frac{(x-x') + (\eta-z')\eta_x}{(x-x')^2+(\eta-z')^2} f(x',z')\,\mathrm{d}x'\mathrm{d}z' + \frac{1}{\pi}\int_{-h}^{\eta'}\int_{-\infty}^{\infty}\frac{(x-x') + (2h+\eta+z')\eta_x}{(x-x')^2+(2h+\eta+z')^2} f(x',z')\,\mathrm{d}x'\mathrm{d}z'. \tag{B 4}$$

Equation (B 1) is a Fredholm integral equation of the second kind with a diagonally dominant structure that can efficiently be solved using an iterative Neumann scheme. Starting from initial guess, $u_n^{(0)} = \mathscr{L}^{(2)}[u_s] + \mathscr{L}^{(3)}[\Omega]$, the normal velocity is iteratively updated using

$$u_n^{(j+1)} = \mathscr{L}^{(1)}[u_n^{(j)}] + \mathscr{L}^{(2)}[u_s] + \mathscr{L}^{(3)}[\Omega] \tag{B 5}$$

until the norm difference between $u_n^{(j+1)}$ and $u_n^{(j)}$ is less than a specified tolerance. Direct numerical integration of the integral operators (B 2)–(B 4) with a simple quadrature rule would require $O(N^2)$ operations, where N is the number of grid points. In addition, components of the kernels related to the free-space Green's function are strongly singular and require special numerical treatment. Since (B 1) has to be inverted at every time step for u_n, direct evaluation of the integrals would be computationally prohibitive for long-term simulations. To speed up evaluation of the convolution integrals, we adopt the approach of Clamond & Grue (2001) and expand the nonlinear kernels of the integral operators as a power series in a wave steepness parameter. We first rewrite the kernels of $\mathscr{L}^{(1)}$ and $\mathscr{L}^{(2)}$ as the product of

https://doi.org/10.1017/S0022112009005850 Published online by Cambridge University Press

nonlinear functions of η and a linear kernel that is independent of η:

$$\begin{aligned}\mathscr{L}^{(1)}[f] = {} & \frac{1}{\pi}\int_{-\infty}^{\infty}\frac{1}{x-x'}\frac{\eta_x f}{1+D^2}\,\mathrm{d}x' - \frac{1}{\pi}\int_{-\infty}^{\infty}\frac{1}{(x-x')^2}\frac{(\eta-\eta')\,f}{1+D^2}\,\mathrm{d}x' \\ & + \frac{1}{\pi}\int_{-\infty}^{\infty}\frac{x-x'}{(x-x')^2+4h^2}\frac{\eta_x f}{1+\tilde{D}^2}\,\mathrm{d}x' \\ & - \frac{1}{\pi}\int_{-\infty}^{\infty}\frac{1}{(x-x')^2+4h^2}\frac{(2h+\eta+\eta')\,f}{1+\tilde{D}^2}\,\mathrm{d}x', \end{aligned} \tag{B 6}$$

$$\begin{aligned}\mathscr{L}^{(2)}[f] = {} & \frac{1}{\pi}\int_{-\infty}^{\infty}\frac{1}{x-x'}\frac{f}{1+D^2}\,\mathrm{d}x' + \frac{1}{\pi}\int_{-\infty}^{\infty}\frac{1}{(x-x')^2}\frac{(\eta-\eta')\eta_x f}{1+D^2}\,\mathrm{d}x' \\ & - \frac{1}{\pi}\int_{-\infty}^{\infty}\frac{x-x'}{(x-x')^2+4h^2}\frac{f}{1+\tilde{D}^2}\,\mathrm{d}x' \\ & + \frac{1}{\pi}\int_{-\infty}^{\infty}\frac{1}{(x-x')^2+4h^2}\frac{(2h+\eta+\eta')\eta_x f}{1+\tilde{D}^2}\,\mathrm{d}x', \end{aligned} \tag{B 7}$$

where $D=(\eta-\eta')/(x-x')$ and $\tilde{D}=\sqrt{(\eta+\eta')^2+4h(\eta+\eta')/(x-x')^2+4h^2}$. Since D and $\tilde{D}$ respectively represent deep- and shallow-water wave steepness parameters (see § 5), the nonlinear term can be expanded as a power series in D:

$$\frac{1}{1+D^2} = \sum_{n=0}^{M}(-1)^n D^{2n} + (-1)^{M+1}\frac{D^{2(M+1)}}{1+D^2}. \tag{B 8}$$

We note that although the series is guaranteed to converge if $D<1$, explicit retention of the remainder term in (B 8) gives one the flexibility to apply (B 8) to cases with $D>1$ through direct numerical integration of the remainder term. However, the singularity of the remainder term increases with increasing powers of M, making its direct integration more difficult. In this paper, we adopt the leading-order approximation to (B 8), i.e.

$$\frac{1}{1+D^2} \approx 1-D^2. \tag{B 9}$$

The FFT method is then used to evaluate the convolution integrals up to $O(D^2)$. Retention of terms up to $O(D^2)$ in the power series expansion ensures that the dominant four-wave nonlinear interactions in deep water are accurately evaluated using the FFT method. Substituting (B 9) into (B 6) and (B 7) and applying the Fourier transform and convolution theorem defined in (3.16) and (3.17) respectively, (B 6) and (B 7) reduce to

$$\begin{aligned}\mathscr{L}^{(1)}[u_n] = {} & -\mathscr{F}^{-1}[\mathrm{e}^{-2kh}\mathscr{F}(u_n)] + \eta\mathscr{F}^{-1}[k(\mathrm{e}^{-2kh}+1)\mathscr{F}(u_n)] \\ & + \mathscr{F}^{-1}[k(\mathrm{e}^{-2kh}-1)\mathscr{F}(u_n\eta)] + \eta^2\mathscr{F}^{-1}\left[\frac{3\mathrm{e}^{-2kh}}{8h^2}(2kh+1)\,\mathscr{F}(u_n)\right] \\ & - 2\eta\mathscr{F}^{-1}\left[\frac{3\mathrm{e}^{-2kh}}{8h^2}(2kh+1)\,\mathscr{F}(u_n\eta)\right] + \mathscr{F}^{-1}\left[\frac{3\mathrm{e}^{-2kh}}{8h^2}(2kh+1)\mathscr{F}(u_n\eta^2)\right] \\ & + \eta_x\mathscr{F}^{-1}[-\mathrm{i}(\mathrm{e}^{-2kh}+1)\mathscr{F}(u_n)] + \eta_x\mathscr{F}^{-1}[\mathrm{i}k\mathrm{e}^{-2kh}\mathscr{F}(u_n\eta)] \\ & + \eta\eta_x\mathscr{F}^{-1}[\mathrm{i}k\mathrm{e}^{-2kh}\mathscr{F}(u_n)], \end{aligned} \tag{B 10}$$

https://doi.org/10.1017/S0022112009005850 Published online by Cambridge University Press

$$\begin{aligned}\mathscr{L}^{(2)}[u_s] &= \mathscr{F}^{-1}[-\mathrm{i}(1-\mathrm{e}^{-2kh})\mathscr{F}(u_s)] \\ &+ \eta\mathscr{F}^{-1}[-\mathrm{i}k\mathrm{e}^{-2kh}\mathscr{F}(u_s)] + \mathscr{F}^{-1}[-\mathrm{i}k\mathrm{e}^{-2kh}\mathscr{F}(u_s\eta)] \\ &+ \eta_x\mathscr{F}^{-1}[-\mathrm{e}^{-2kh}\mathscr{F}(u_s)] + \eta^2\mathscr{F}^{-1}\left[-\mathrm{i}\frac{k^2}{2}\left(\frac{\mathrm{e}^{-2kh}}{2kh}+1\right)\mathscr{F}(u_s)\right] \\ &+ 2\eta\mathscr{F}^{-1}\left[\mathrm{i}\frac{k^2}{2}\left(\frac{\mathrm{e}^{-2kh}}{2kh}+1\right)\mathscr{F}(u_s\eta)\right] + \mathscr{F}^{-1}\left[-\mathrm{i}\frac{k^2}{2}\left(\frac{\mathrm{e}^{-2kh}}{2kh}+1\right)\mathscr{F}(u_s\eta^2)\right] \\ &+ \eta\eta_x\mathscr{F}^{-1}[k(\mathrm{e}^{-2kh}-1)\mathscr{F}(u_s)] + \eta_x\mathscr{F}^{-1}[k(\mathrm{e}^{-2kh}+1)\mathscr{F}(u_s\eta)]. \qquad \text{(B 11)}\end{aligned}$$

In infinitely deep water ($h \to \infty$), the Fourier-based integral operators further reduce to

$$\mathscr{L}^{(1)}[u_n] = \eta\mathscr{F}^{-1}[k\mathscr{F}(u_n)] - \mathscr{F}^{-1}[k\mathscr{F}(u_n\eta)] + \eta_x\mathscr{F}^{-1}[-\mathrm{i}\mathscr{F}(u_n)], \qquad \text{(B 12)}$$

$$\begin{aligned}\mathscr{L}^{(2)}[u_s] &= \mathscr{F}^{-1}[-\mathrm{i}\mathscr{F}(u_s)] + \mathscr{F}^{-1}\left[-\mathrm{i}\frac{k^2}{2}\mathscr{F}(u_s\eta^2)\right] + 2\eta\mathscr{F}^{-1}\left[\mathrm{i}\frac{k^2}{2}\mathscr{F}(u_s\eta)\right] \\ &+ \eta^2\mathscr{F}^{-1}\left[-\mathrm{i}\frac{k^2}{2}\mathscr{F}(u_s)\right] + \eta_x\mathscr{F}^{-1}[k\mathscr{F}(u_s\eta)] - \eta\eta_x\mathscr{F}^{-1}[k\mathscr{F}(u_s)]. \qquad \text{(B 13)}\end{aligned}$$

The deep-water operators (B 12) and (B 13) are identical to those derived by Craig & Sulem (1993) using a Taylor series expansion of the Dirichlet to Neumann operator.

The vorticity-related operator $\mathscr{L}^{(3)}$ includes nonlinear contributions from both the kernel function as well as vertical integration to the instantaneous free surface. We consider deep-water applications and modify the vertical profile of the vorticity field defined in (5.9) up to the free surface,

$$\hat{\Omega}(k,\ z) = -\mathrm{e}^{k(z-\eta')}\hat{\eta}(k)U''(z). \qquad \text{(B 14)}$$

Applying the convolution theorem to (B 4) and substituting (B 14) for the vorticity field, we obtain

$$\begin{aligned}\mathscr{L}^{(3)}[\Omega] &= \mathscr{F}^{-1}\left[-\mathrm{i}\hat{\eta}(k)\int_{-\infty}^{\eta'}\mathrm{e}^{2kz'-k(\eta+\eta')}U''(z')\mathrm{d}z'\right] \\ &- \eta_x\mathscr{F}^{-1}\left[\hat{\eta}(k)\int_{-\infty}^{\eta'}\mathrm{e}^{2kz'-k(\eta+\eta')}U''(z')\,\mathrm{d}z'\right]. \qquad \text{(B 15)}\end{aligned}$$

For an exponentially sheared current $U(z) = U_0\exp(z/d)$, $\mathscr{L}^{(3)}$ reduces to

$$\mathscr{L}^{(3)}[\Omega] = \mathscr{F}^{-1}\left[-\mathrm{i}\frac{U_{\eta'}}{d\,(1+2kd)}\mathrm{e}^{k(\eta'-\eta)}\hat{\eta}\right] - \eta_x\mathscr{F}^{-1}\left[\frac{U_{\eta'}}{d\,(1+2kd)}\mathrm{e}^{k(\eta'-\eta)}\hat{\eta}\right]. \qquad \text{(B 16)}$$

Expanding the exponential term in powers of wave steepness and retaining terms up to $O[(k\eta)^3)]$ yields

$$\begin{aligned}\mathscr{L}^{(3)}[\Omega] &= \mathscr{F}^{-1}\left[-\mathrm{i}\frac{1}{d\,(1+2kd)}\left[\mathscr{F}\,(U_\eta\eta) + k\mathscr{F}\,(U_\eta\eta^2) + \frac{k^2}{2}\mathscr{F}\,(U_\eta\eta^3)\right]\right] \\ &- \eta\mathscr{F}^{-1}\left[-\mathrm{i}\frac{k}{d\,(1+2kd)}\left[\mathscr{F}\,(U_\eta\eta) + k\mathscr{F}\,(U_\eta\eta^2)\right]\right] \\ &+ \eta^2\mathscr{F}^{-1}\left[-\mathrm{i}\frac{k^2}{2d\,(1+2kd)}\mathscr{F}\,(U_\eta\eta)\right] + \eta\eta_x\mathscr{F}^{-1}\left[\frac{k}{d\,(1+2kd)}\mathscr{F}\,(U_\eta\eta)\right] \\ &- \eta_x\mathscr{F}^{-1}\left[\frac{1}{d\,(1+2kd)}\left[\mathscr{F}\,(U_\eta\eta) + k\mathscr{F}\,(U_\eta\eta^2)\right]\right]. \qquad \text{(B 17)}\end{aligned}$$

https://doi.org/10.1017/S0022112009005850 Published online by Cambridge University Press

REFERENCES

Baker, G. R., Meiron, D. I. & Orszag, S. A. 1982 Generalized vortex methods for free-surface flow problems. *J. Fluid Mech.* **123**, 477–501.

Baker, G. R., Meiron, D. I. & Orszag, S. A. 1989 Generalized vortex methods for free-surface flow problems. Part 2. Radiating waves. *J. Sci. Comp.* **4**, 237–259.

Banner, M. L. & Tian, X. 1998 On the determination of the onset of breaking for modulating surface gravity water waves. *J. Fluid Mech.* **367**, 107–137.

Baumstein, A. I. 1998 Modulation of gravity waves with shear in water. *Stud. Appl. Math.* **100**, 365–390.

Benjamin, T. B. 1962 The solitary wave on a stream with an arbitrary distribution of vorticity. *J. Fluid Mech.* **12**, 97–116.

Benjamin, T. B. & Feir, J. E. 1967 The disintegration of wave trains on deep water. Part 1. Theory. *J. Fluid Mech.* **27**, 417–430.

Biesel, F. 1950 Etude theorique de la houle en eau courante. *Houille Blan.* **5**, 279–285.

Bliven, L. F., Huang, N. E. & Long, S. R. 1986 Experimental study of the influence of wind on Benjamin–Feir sideband instability. *J. Fluid Mech.* **162**, 237–260.

Brevik, I. 1979 Higher-order waves propagating on constant vorticity currents in deep water. *Coastal Engng* **2**, 237–259.

Chen, L. & Vorus, W. S. 1992 Application of a vortex method to free surface flows. *Intl J. Num. Meth. Fluids* **14**, 1289–1310

Choi, W. 1995 Nonlinear evolution equations for two-dimensional surface waves in a fluid of finite depth. *J. Fluid Mech.* **295**, 381–394.

Clamond, D., Fructus, D., Grue, J. & Kristiansen, O. 2005 An efficient model for three-dimensional surface wave simulations. Part 2. Generation and absorption. *J. Comput. Phys.* **205**, 686–705.

Clamond, D. & Grue, J. 2001 A fast method for fully nonlinear water-wave computations. *J. Fluid Mech.* **447**, 337–355.

Craig, W. & Sulem, C. 1993 Numerical simulation of gravity waves. *J. Comput. Phys.* **108**, 73–83.

Crapper, G. D. 1972 Nonlinear gravity waves on steady non-uniform currents. *J. Fluid Mech.* **52**, 713–724.

Crawford, D. R., Lake, B. M., Saffman, P. G. & Yuen, H. C. 1981 Stability of weakly nonlinear deep-water waves in two and three dimensions. *J. Fluid Mech.* **105**, 177–191.

Dold, J. W. 1992 An efficient surface-integral algorithm applied to unsteady gravity waves. *J. Comput. Phys.* **103**, 90–115.

Dalrymple, R. A. 1974 A finite amplitude wave on a linear shear current. *J. Geophys. Res.* **79**, 4498–4504.

Dalrymple, R. A. 1977 A numerical model for periodic finite amplitude waves on a rotational fluid. *J. Comput. Phys.* **24**, 29–44.

Dommermuth, D. G. & Yue, D. K. P. 1987 A high-order spectral method for the study of nonlinear gravity waves. *J. Fluid Mech.* **184**, 267–288.

Dysthe, K., Krogstad, H. E. & Muller, P. 2008 Oceanic rogue waves. *Annu. Rev. Fluid Mech.* **40**, 287–310.

Freeman, N. C. & Johnson, R. S. 1970 Shallow water waves on shear flows. *J. Fluid Mech.* **42**, 401–409.

Fructus, D., Clamond, D., Grue, J. & Kristiansen, O. 2005 An efficient model for three-dimensional surface wave simulations. Part 1. Free space problems. *J. Comput. Phys.* **205**, 665–685.

Gerber, M. 1987 The Benjamin–Feir instability of a deep-water Stokes wavepacket in the presence of a non-uniform medium. *J. Fluid Mech.* **176**, 311–332.

Hou, T. Y., Hu, G. & Zhang, P. 2003 Singularity formation in three-dimensional vortex sheets. *Phys. Fluids.* **15**, 147–172.

Jonsson, I. G. 1990 Wave–current interactions. In *The Sea* (ed. B. Le Mehaute and D. M. Hanes), pp. 65–120. John Wiley.

Kirby, J. T. & Chen, T. M. 1989 Surface waves on vertically sheared flows: approximate dispersion relations. *J. Geophys. Res.* **94**, 1013–1027.

https://doi.org/10.1017/S0022112009005850 Published online by Cambridge University Press

Kishida, N. & Sobey, R. J. 1988 Stokes theory for waves on a linear shear current. *J. Engng Mech.* **114**, 1317–1334.

Kharif, C. & Pelinovsky, E. 2003 Physical mechanisms of the rogue wave phenomenon. *Eur. J. Mech.* B **22**, 603–634.

Ko, J. & Krauss, W. 2008 Effect of vorticity on steady water waves. *J. Fluid Mech.* **608**, 197–215.

Landrini, M., Oshri, O., Waseda, T. & Tulin, M. P. 1998 Long time evolution of gravity wave systems. In *Proc. 13th Intl Workshop on Water Waves and Floating Bodies*, Alphen aan den Rijn, The Netherlands.

Li, J. C., Hui, W. H. & Donelan, M. A. 1988 Effects of velocity shear on the stability of surface deep water wave trains. In *Nonlinear Water Waves* (ed. K. Horikawa & H. Maruo), pp. 213–220. Springer.

Longuet-Higgins, M. S. 1975 Integral properties of periodic gravity waves of finite amplitude. *Proc. R. Soc. Lond.* A **342**, 157–174.

Longuet-Higgins, M. S. & Cokelet E. D. 1976 The deformation of steep surface waves on water. Part 1. A numerical method of computation. *Proc. R. Soc. Lond.* A **350**, 1–26.

Longuet-Higgins, M. S. & Stewart R. W. 1961 The changes in amplitude of short gravity waves on steady non-uniform currents. *J. Fluid Mech.* **10**, 529–549.

Madsen, P. A., Bingham, H. B. & Liu, H. 2002 A new Boussinesq method for fully nonlinear waves from shallow to deep water. *J. Fluid Mech.* **462**, 1–30.

McDonald, B. E. & Witting, J. M. 1984. A conservation law related to Kelvin's circulation theorem. *J. Comput. Phys.* **56**, 237–243.

Morino, L., Salvatore, F. & Gennaretti, M. 1999 A new velocity decomposition for viscous flows: Lighthill's equivalent-source method revisited. *Comp. Meth. App. Mech. Engng* **173**, 317–336

Morse, P. M. & Feshbach, H. 1953 *Methods of Theoretical Physics*. McGraw-Hill.

Nwogu, O. 1993 Alternative form of Boussinesq equations for nearshore wave propagation. *J. Waterway Port Coastal Ocean Engng* ASCE **119**, 618–638.

Peregrine, D. H. 1976 Interaction of water waves and currents. *Adv. Appl. Mech.* **16**, 9–117.

Peregrine, D. H. & Thomas, G. P. 1979 Finite-amplitude deep-water waves on currents. *Phil. Trans. R. Soc. Lond.* A **292**, 371–390.

Shen, C. Y. 2001 Constituent Boussinesq equations for waves and currents. *J. Phys. Ocean.* **31**, 850–859.

Shrira, V. I. 1993 Surface waves on shear currents: solution of the boundary-value problem. *J. Fluid Mech.* **252**, 565–584.

Simmen, J. A. & Saffman, P. G. 1985 Steady deep-water waves on a linear shear current. *Stud. Appl. Math.* **75**, 35–57.

Skop, R. A. 1987 An approach to the analysis of the interaction of surface waves with depth-varying current fields. *App. Math. Modelling.* **11**, 432–437.

Stewart, R. H. & Joy. J. W. 1974 HF radio measurements of surface currents. *Deep Sea Res.* **21**, 1039–1049.

Swan, C., Cummins, I. P. & James, R. L. 2001 An experimental study of two-dimensional surface water waves propagating on depth-varying currents. Part 1. Regular waves. *J. Fluid Mech.* **428**, 273–304.

Swan, C. & James, R. L. 2001 A simple analytical model for surface water waves on a depth-varying current. *Appl. Ocean Res.* **22**, 331–347

Teles, Da Silva, A. F. & Peregrine, D. H. 1988 Steep surface waves on water of finite depth with constant vorticity. *J. Fluid Mech.* **195**, 281–302.

Thomas, G. P. 1990 Wave–current interactions: an experimental and numerical study. Part 2. Nonlinear waves. *J. Fluid Mech.* **216**, 505–536.

Thompson, P. D. 1949 The propagation of small surface disturbances through rotational flow. *Ann. N. Y. Acad. Sci.* **51**, 463–474.

Tsao, S. 1959 Behaviour of surface waves on a linearly varying flow. *Tr. Mosk. Fiz.-Tekh. Inst. Issled. Mekh. Prikl. Mat.* **3**, 66–84.

Vinje, T. & Brevig, P. 1981 Numerical simulation of breaking waves. *Adv. Water Res.* **4**, 77–82.

Waseda, T. & Tulin, M. P. 1999 Experimental study of the stability of deep-water wave trains including wind effects. *J. Fluid Mech.* **401**, 55–84.

https://doi.org/10.1017/S0022112009005850 Published online by Cambridge University Press

Wehausen, J. V. & Laitone, E. V. 1960 Surface waves. In *Handbuch der Physik*, vol. 9, pp. 446–778. Springer.

Wei, G., Kirby, J. T. & Sinha, A. 1999 Generation of waves in Boussinesq models using a source function method. *Coastal Engng* **36**, 271–299.

West, B. J., Brueckner, K. A., Janda, R. S., Milder, D. M. & Milton, R. L. 1987 A new numerical method for surface hydrodynamics. *J. Geophys. Res.* **92**, 11803–11824.

Whitham, G. B. 1965 A general approach to linear and nonlinear dispersive waves using a Lagrangian. *J. Fluid Mech.* **22**, 273–283.

Wu, J. C. 1984 Fundamental solutions and numerical methods for flow problems. *Intl J. Num. Meth. Fluids* **4**, 185–201.

Zakharov, V. E. 1968 Stability of periodic waves of finite amplitude on the surface of a deep fluid. *Zh. Prikl. Mekh. Tekh. Fiz*. **9**, 86–94.

Zakharov V. E., Dyachenko, A. I. & Vasilyev, O. A. 2002 New method for numerical simulation of a nonstationary potential flow of incompressible fluid with a free surface. *Eur. J. Mech.* B **21**, 283–291

Zaroodny, S. J. & Greenberg, M. D. 1973 On a vortex sheet approach to the numerical calculation of water waves. *J. Comput. Phys.* **11**, 440–446.

https://doi.org/10.1017/S0022112009005850 Published online by Cambridge University Press